corrosion and materials degradation

MDPI

Article

Investigation via Electron Microscopy and Electrochemical Impedance Spectroscopy of the Effect of Aqueous Zinc Ions on Passivity and the Surface Films of Alloy 600 in PWR PW at 320 °C

Yifan Jiang [1], Karen C. Bustillo [2] and Thomas M. Devine [1,*]

[1] Department of Materials Science and Engineering, University of California, Berkeley, CA 94720, USA
[2] National Center for Electron Microscopy, Molecular Foundry, Lawrence Berkeley National Laboratory, Berkeley, CA 94720, USA
* Correspondence: devine@berkeley.edu

Abstract: Aqueous zinc ions lower the corrosion rate of Alloy 600, which helps lower the radiation dose rate in pressurized water reactors (PWRs). The influence of zinc on the electrochemical behavior of Alloy 600 in PWR primary water (PW) at 320 °C was investigated using a combination of electron microscopy and electrochemical impedance spectroscopy (EIS). Secondary electron microscopy (SEM) and scanning transmission electron microscopy (STEM)/energy-dispersive X-ray spectroscopy (EDS) indicated duplex surface films were formed on the Alloy 600 in PWR PW with and without 100 ppb of zinc. There was no effect of zinc on the chromium-rich inner layer (IL) (of Cr_2O_3 and/or CrOOH). Zinc had a significant effect on the outer layer (OL). In the absence of zinc, a highly porous OL formed that was mostly composed of nickel oxide whiskers. In the presence of zinc, a zinc-containing, denser OL of oxide was formed. The EIS data were acquired in laboratory simulated PWR PW at 320 °C with and without 100 ppb zinc. The spectra were measured at nine different values of potential that spanned a 500 mV-wide range. The EIS indicated there was no effect of zinc on the oxidation rate of metals at the alloy/IL interface nor on the transport of ions through the IL. Zinc lowered the corrosion rate because the dense OL inhibited the release of nickel ions from the IL into the solution.

Keywords: passive film; Alloy 600; pressurized water reactor primary water with zinc; electrochemical impedance spectroscopy; scanning transmission electron microcopy; energy-dispersive spectroscopy

Citation: Jiang, Y.; Bustillo, K.C.; Devine, T.M. Investigation via Electron Microscopy and Electrochemical Impedance Spectroscopy of the Effect of Aqueous Zinc Ions on Passivity and the Surface Films of Alloy 600 in PWR PW at 320 °C. *Corros. Mater. Degrad.* **2023**, *4*, 54–89. https://doi.org/10.3390/cmd4010005

Academic Editor: Richard Barker

Received: 14 October 2022
Revised: 17 December 2022
Accepted: 6 January 2023
Published: 19 January 2023

1. Introduction

As of 2017 there were over 90 pressurized water reactors (PWRs), which represented 36% of the worldwide total of nuclear reactors. In the U.S., 40% of these PWRs inject zinc into the primary water (PW) to mitigate metal degradation of the reactor components [1]. The metal is usually a nickel-rich alloy known as Alloy 600, and the degradation can occur in a number of applications such as steam generator tubes, control rod drive nozzles in the reactor vessel head, and instrument nozzles in the bottom head. Zinc ions in the PW of PWRs have been shown to have three positive effects on the performance of Alloy 600. First, zinc ions dramatically lower radiation emitted from the Alloy 600 in PWRs [2–6]; This effect has occurred in boiling water reactors (BWRs) as well [7]. The radiation occurred in part because nickel in the alloy was oxidized, dissolved into the PW, and transmuted to ^{60}Co when deposited onto the fuel cladding. ^{60}Co released from the cladding surface re-entered the PW. From there, the ^{60}Co was incorporated into the oxides on the interior surfaces of numerous reactor components. The radiation emitted by ^{60}Co poses a threat to workers performing inspections and preventative maintenance of the reactor. Second, zinc ions lower the corrosion rate of Alloy 600 [8–10]. The lower corrosion rate has little influence on the structural integrity of components because Alloy 600's corrosion rate is already low in PWR PW. The major benefit of the lower oxidation rate is the lower radiation dose rate associated with the reduced amount of nickel ions in the PW. Third, zinc ions

increase the resistance of Alloy 600 to stress corrosion cracking (SCC) in PWRs [11–14] and BWRs [15–17]. All three effects are dependent on the fundamental electrochemical behavior of Alloy 600 and on the surface films that form on Alloy 600. Due to the importance of zinc's lowering of the radiation dose rate and the role in corrosion of Alloy 600 of the radiation dose rate, our investigation was focused on understanding how zinc lowers the oxidation rate of Alloy 600.

In the present paper, we investigated Alloy 600's electrochemical behavior and its surface films using a combination of electrochemical impedance spectroscopy (EIS) and electron microscopy. Our study investigated the effect of zinc by comparing the results of tests conducted in PWR PW with zinc to the results of tests conducted in PWR PW without zinc. Consequently, it will be helpful to briefly review earlier investigations of the surface films formed on Alloy 600 in PWR PW without zinc.

Earlier research demonstrated that there was no single surface film of Alloy 600 in zinc-free PW. Various studies have shown that the surface film that formed on Alloy 600 in PWR PW evolved with time and was a function of temperature [18–22], pH [22,23], the electrolyte composition [22,24], and the potential [18,25,26] (including the partial pressures of hydrogen [27–30] and oxygen [31,32]).

Although many of the qualities of the surface film have a time dependence, the presence of both an inner layer (IL) and an outer layer (OL) is known to be time-independent. In two reports, the surface films of Alloy 600 in PWR PW at 325 °C exhibited a duplex structure at all times of immersion, even for times as short as 0.4 min [33] and on samples that were simply heated to 320 °C and immediately cooled to room temperature [34]. A duplex structure was also present after hundreds to thousands of hours of immersion. There was a general consensus among all of the investigators that the IL was Cr-rich and the OL was Ni-rich. The IL was of interest to us because it functioned as a barrier layer and the OL was of interest because, as shown in the present study, it too affected the electrochemical behavior.

There is a lack of consensus, however, regarding the time dependance of the composition of the IL. A previous report showed that after very short periods of immersion, there was selective dissolution of Ni and Fe and formation of the IL of Cr_2O_3 [34]. Immersion times between 0.4 min and 4 min resulted in a 1 nm-thick IL of Cr_2O_3 and an outer surface of CrOOH, as well as islands of $Ni(OH)_2$ that formed on top of the IL [33]. From 4 min to 8 min, the IL of Cr_2O_3 thickened and CrOOH vanished from the outer surface, which was now covered by $Ni(OH)_2$ [33]. In another report that was in agreement with Machet et al. [34], Voyshnis et al. [35] reported an IL of Cr_2O_3 after 1 min of immersion and a few islands of $NiCr_2O_4$ at the interface of the IL/alloy. An OL was also present after 1 min of immersion that was rich in Fe and Ni. The film thickened with time but its structure was the same at 1 h as at 1 min. Between 1 h and 5 h, significant changes occurred to the IL. At 5 h, the IL consisted of $NiCr_2O_4$ with a few islands of Cr_2O_3. The transition of the IL from Cr_2O_3 to $NiCr_2O_4$ after just several hours of immersion conflicted with the results of Panter et al., who found an IL of Cr_2O_3 at immersion times of 300 h.

An IL of $NiCr_2O_4$ was also found in the duplex film on Alloy 600 in laboratory tests of 1000–10,000 h [9] and in the duplex film on Alloy 600 tubes that were in service in PWR PW for thousands of hours [4], which suggested that the steady-state structure consisted of a duplex film with an IL of $NiCr_2O_4$. Such a steady-state IL of $NiCr_2O_4$ was consistent with the calculations of Kauffman, who showed that $NiCr_2O_4$ was the thermodynamically stable form of Alloy 600 in PWR PW [36].

Our focus on relatively short times of immersion was driven by the lack of consensus among earlier results that investigated the film's evolution with time. A portion of our tests were conducted for an immersion time of 4 h, which was within the gap between 1 h and 5 h in which one study [35] found the IL changed from Cr_2O_3 to $NiCr_2O_4$. To our knowledge, no other studies have been conducted on samples immersed for 4 h. We also investigated immersion times up to 60 h. Furthermore, as in several other investigations [18,25,26,32], we conducted tests at a series of applied potentials because Alloy 600 is used for a number

of components located throughout the PWR and exhibits different corrosion potentials at different locations [1]. A significant number of microscopy investigations of the surface film that forms on Alloy 600 [3,12,24,27,31,33,34,37] as well as a number of EIS studies [18,32,38] have been performed. Peng et al. [28] employed the two techniques in their investigation of Alloy 600 after 500 h of immersion in high-purity water at 288 °C. In our study, we intimately integrated the two techniques by using the results of electron microscopy to interpret the EIS.

The present results contributed to our understanding of how the surface film of Alloy 600 depends on potential and evolves with time as well as how zinc lowers the corrosion rate of Alloy 600.

2. Materials and Methods

2.1. Materials and High-Temperature, High-Pressure Test Facility

Steam generator tubing composed of Alloy 600 (Ni-15Cr-8Fe) (provided by Peter Andresen (Ret.) of GE-GRC) was cut into rectangular coupons of 0.7 cm × 0.7 cm × 0.08 cm. Each sample was ground with SiC paper up to 1200 grit and polished using 1 µm diamond paste. The coupon was spot welded to a commercial Alloy 600 wire, which was then shielded with a PTFE tubing and an outer ceramic tube insulator.

An in-house-built single flow-through system was used in order to keep the solution concentration constant during each test. The aqueous solution contained 1200 ppm B and 2 ppm Li, thereby simulating the conventional concentration of these elements in primary water. The solution was prepared with 18.8 MΩ deionized water and analytical-grade chemicals. The premixed solution was deaerated using ultra-high purity grade $N_{2(g)}$ for 48 h and then passed through two 150 cm-long vertical columns with a counter flow of N_2- 4% H_2 forming gas. The aqueous solution was then pressurized and pumped through a heat exchanger into an autoclave that was kept at 320 °C and 1800 psi. The solution that exited the autoclave was released to an air atmosphere and disposed. The autoclave body and the water tubing exposed to high temperature and high pressure were all composed of Grade II titanium to avoid Ni^{2+}, $Fe^{2+/3+}$, and Cr^{3+} release from the water loop and autoclave. The segments of water tubing that operated at room temperature were composed of 304 stainless steel.

A Pt mesh served as the counter electrode. A Pt wire served as the substrate of the reversible hydrogen reference electrode (RHE). All potentials are reported vs. the standard hydrogen electrode (SHE). All electrodes were sealed through the autoclave and connected to a Gamry PC4/750 potentiostat for in situ electrochemical measurements.

2.2. Electrochemical Measurements

The following procedure was used for both water conditions (with 100 ppb of Zn added and without added Zn).

The working electrode was polarized cathodically at −1.923 V vs. SHE (i.e., −1.2 V vs. reference electrode = reversible hydrogen electrode) during heating of the temperature of the electrolyte in the autoclave from room temperature to 320 °C. The objective of the cathodic polarization was to remove some/all of the air-formed oxide and to inhibit oxide formation during heating. Potentiodynamic scans in which the potential of the working electrode of Alloy 600 was increased from −1.923 V vs. SHE to +0.777 V at 1 mV/s were conducted to characterize the general electrochemical behavior of Alloy 600.

Two sets of potentiostatic electrochemical impedance spectroscopy (EIS) data were measured. In the first set, samples were cathodically polarized at −1.923 V as the autoclave was heated from room temperature to 320 °C. The potentiostat was then shut off and the sample rested in an open circuit for 48 h. The EIS was then conducted at one of two values of potential (one value of potential per sample). Specifically, after 48 h at the open circuit potential, the sample was polarized for 4 h at close to −700 mV (−695 mV no−Zn and −690 mV with-Zn) or close to −550 mV (−565 mV no-Zn and −570 mV with-Zn), and then the EIS data were obtained. The EIS was conducted from 50 kHz to 3 mHz with a

10 mV AC signal, and the duration of the test was approximately three hours. After each measurement of the EIS, the autoclave was cooled to room temperature. Then, the sample of Alloy 600 was removed and dried, and its surface film, which formed during the 48 h in an open circuit plus a total of seven hours at either ~−700 mV or ~−550 mV, was examined via electron microscopy as described in the following Section 2.3.

The EIS data measured at close to −700 mV and close to −550 mV differed significantly. To better define the potential dependency, a second set of EIS was conducted at discreet potentials of $-743\ mV_{SHE}$, $-723\ mV_{SHE}$, $-673\ mV_{SHE}$, $-623\ mV_{SHE}$, $-573\ mV_{SHE}$, $-523\ mV_{SHE}$, $-423\ mV_{SHE}$, and $-223\ mV_{SHE}$. Specifically, a single sample was cathodically polarized at −1.923 V during heating from room temperature to 320 °C. At 320 °C, the sample's potential was stepped to −743 mV and held at that value for 4 h, and then the EIS was measured. After the three-hour-long measurement via EIS, the sample's potential was stepped to a new value and held for 4 h, and then the EIS was measured. The procedure was repeated at a total of nine values of potential: $-743\ mV_{SHE}$, $-723\ mV_{SHE}$, $-673\ mV_{SHE}$, $-623\ mV_{SHE}$, $-573\ mV_{SHE}$, $-523\ mV_{SHE}$, $-423\ mV_{SHE}$, −323 mV and $-223\ mV_{SHE}$. After the EIS was conducted at −223 mV, the autoclave was cooled to room temperature. The sample was removed from the autoclave and dried, and the surface film was investigated via electron microscopy (see Section 2.3). This sample was labeled as −223 mV.

The steady-state condition of the EIS was demonstrated by the measurement from 2 mHz to 50 kHz exactly matching the measurement from 50 kHz to 2 mHz. The validity of the measured EIS data was confirmed via Kramers–Kronig transforms.

2.3. SEM and TEM/EDS

Surface films of samples from the first set of measurements via EIS at −695 mV (No-Zn), −565 mV (No-Zn), −690 mV (with Zn), and −570 mV (with Zn), as well as the two samples from the second set of EIS in which the EIS was conducted at nine different potentials, were investigated for both water conditions, thereby resulting in six SEM/TEM samples. Because the EIS results indicated that the EIS was practically independent of the history of the potential prior to the testing potential, this last sample was labeled at the final potential of −223 mV. Cross-sections through the surface film and alloy substrate were prepared for TEM samples using the dual-beam focused ion beam (FIB) of an FEI Strata 235. Prior to cutting, platinum was deposited onto the surface film for protection before each TEM lift-out sample was prepared with the Omniprobe system. An FEI TitanX 60-300 microscope was used for EDS analyses of the oxide films to investigate their chemical compositions. The TEM/EDS experiments were all conducted at 200 kV. The TEM/EDS results were used to help interpret the results of the EIS measurements.

3. Results

We combined electrochemical tests and electron microscopy to investigate the effect of aqueous zinc ions on the corrosion behavior of Alloy 600. The results of electron microscopy are presented first because they greatly facilitated the analyses of the EIS.

3.1. Electron Microscopy

SEM revealed the structures of the outer layers on a global scale. TEM dark-field cross-sectional images of the duplex surface film furnished structural information of the inner layer (IL) and outer layer (OL). STEM/EDS provided compositional information, in particular the variation in composition with position in the surface film and in the alloy.

3.1.1. Outer Layer—SEM Results

As concluded in the Discussion section, the OL was responsible for much of the effect of zinc on the electrochemical behavior of Alloy 600.

The surfaces of samples of Alloy 600 following polarization at −695 mV, −565 mV, and −223 mV in zinc-free, 320 °C PWR PW are shown in the scanning electron micrographs presented in Figure 1a,b,c, respectively. The most notable feature was the large number

of whiskers in samples polarized at −695 mV and −565 mV and the reduced number and shorter lengths of whiskers in the sample polarized in 50 mV increments from −743 mV to −223 mV. The formation of whiskers of NiO on Alloy 600 [39,40] and on Alloy 690 [24] were reported in earlier investigations.

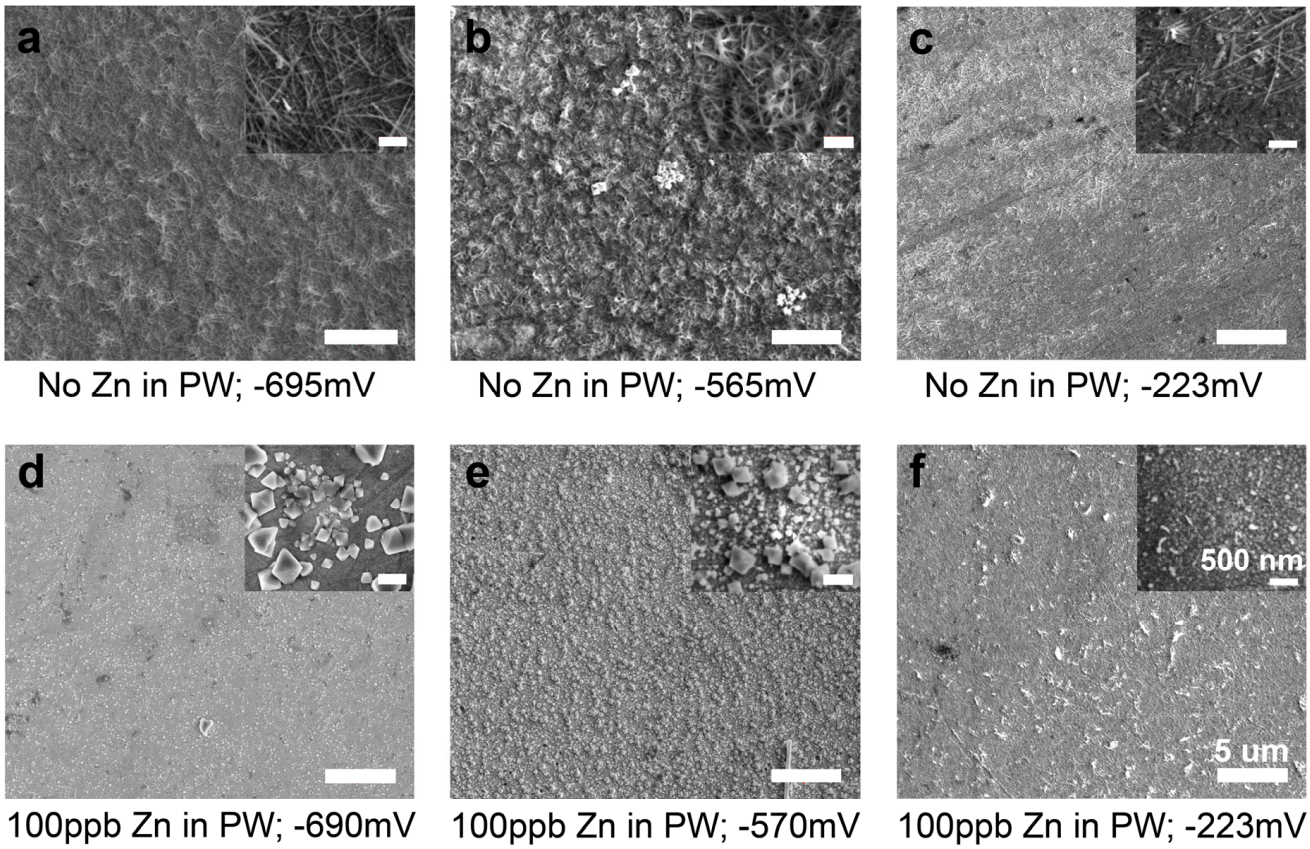

Figure 1. Scanning electron micrographs of surface films formed on Alloy 600 polarized in PWR PW at 320 °C without zinc at a potential of (**a**) −695 mV, (**b**) −565 mV, and (**c**) −223 mV. Scanning electron micrographs of surface films formed on Alloy 600 polarized in PWR PW at 320 °C with 100 ppb of zinc at a potential of (**d**) −690 mV, (**e**) −570 mV, and (**f**) −223 mV. The scale bar is 500 nm for the inset and 5 μm for the larger field of view.

As shown in the scanning electron micrographs in Figure 1d,e, the samples polarized at −690 mV and −570 mV in PWR PW with 100 ppb of zinc were completely free of whiskers, which was in marked contrast to the films formed on A600 in PWR PW without zinc. Samples polarized in 50 mV increments from −743 mV to −223 mV were also free of whiskers as shown in Figure 1f. Rather than whiskers, the most apparent structural features were polyhedral particles that ranged in size from 50 nm to 500 nm. There was also a large number density of closely packed particles smaller than 10 nm.

3.1.2. Outer Layer—TEM Results PWR PW no Zn

The TEM cross-sectional images of samples polarized in PWR PW without zinc at −695 mV, −565 mV, and −223 mV are presented in Figures 2a, S1a and S2a, respectively. At −695 mV and −565 mV, the OL was discontinuous with gaps in which the OL was either very thin or did not cover the IL at all. The discontinuous nature of the OL was consistent with the SEM results that showed the OL was largely composed of whiskers.

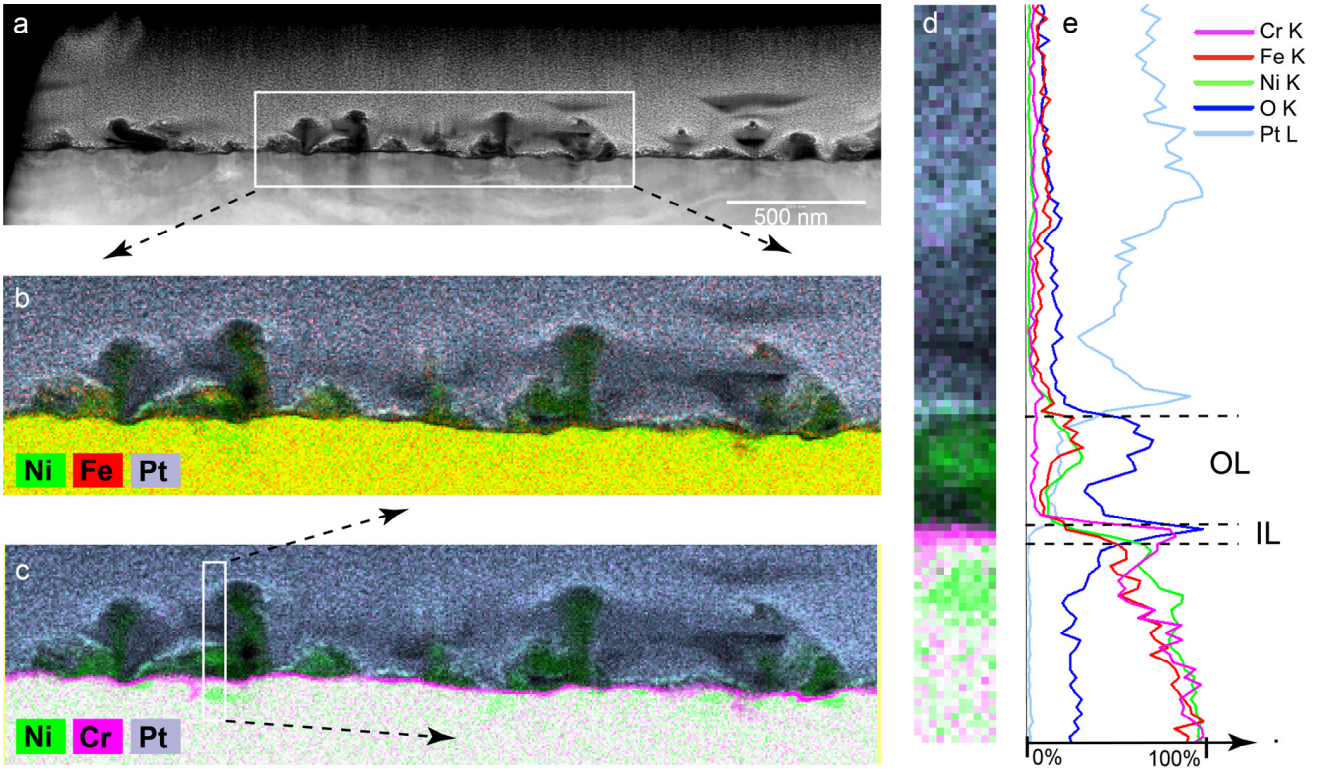

Figure 2. (**a**) Dark-field cross-sectional image of Alloy 600 polarized at −565 mV in PWR PW with no zinc. (**b**) EDS map of nickel, iron, and platinum. (**c**) EDS map of nickel, chromium, and platinum. (**d**) EDS map of region of narrow width pictured in (**c**). (**e**) Integrated intensities of elements in region of narrow width plotted on a scale of 0% to 100% for each element's total X-ray count.

As shown in the SEM image in Figure 1c, the OL that formed following step polarizations in 50 mV increments from −743 mV to −223 mV was more heterogeneous with regions of near-continuous coverage and free of whiskers and locations where whiskers were observed. The cross-sectional TEM sample showed both morphologies in different regions. Figure S2a shows the region with a more compact outer layer providing near continuous coverage of the IL. The whiskers are straight, shorter in length, and fewer in number than those formed at −695 mV and −565 mV.

The EDS maps and linescans presented in Figures 2b–e, S1b–e and S2b–e provide qualitative visualization of the composition. Note that the maximum value of concentration of each linescan was set to 100% for each element; each element was plotted from 0% to 100% of its acquired X-ray counts. For example, the Pt linescan in grey goes from its minimum near 0% in the alloy to its maximum of 100% at one point in the OL. Thus, each color of linescan indicates the amount that that specific element changed along the length of the white boxes (shown in Figures 2c, S1c and S2c). The white boxes traversed the alloy, the IL, the OL, and the Pt overcoat. Each linescan reveals how the element changed with location and thereby defined the position of the IL and OL.

Quantitative measurements of composition were obtained via background subtraction and fitting of peaks with good signal-to-noise ratios. Quantification of the EDS spectrum from the outer-layer pixels indicated that the whiskers were nickel-rich oxide with some iron (as shown in Figure 3 for the −565 mV sample). The outer layer was quantified by outlining the regions in the cross-section that were oxide and summing the EDS spectrum from these pixels in order to achieve a spectrum with a sufficient signal-to-noise ratio to allow a background subtraction and fit the peaks. The quantification was conducted using the Cliff–Lorimer method [41]. While this method holds for thin foils, the X-ray energies of the transition metal k-edges were similar enough that variations in thickness would affect the metal quantification similarly. The quantification of the lower energy X-rays

was affected by the variations in thickness and for this reason, the oxygen quantification was not very accurate. The quantitative compositions of the OLs at all three potentials are summarized in Table 1 (the detailed results are presented in Table S2). The compositions of the OLs and whiskers as a function of potential could not be quantified within the accuracy of the measurement. Despite the presence of nickel-rich whiskers at −695 mV and −565 mV and the reduction in whiskers at −223 mV, the compositions of the OL formed in zinc-free electrolyte at all three values of potential were approximately the same: enriched in nickel and with small amounts of iron and only very small amounts of chromium.

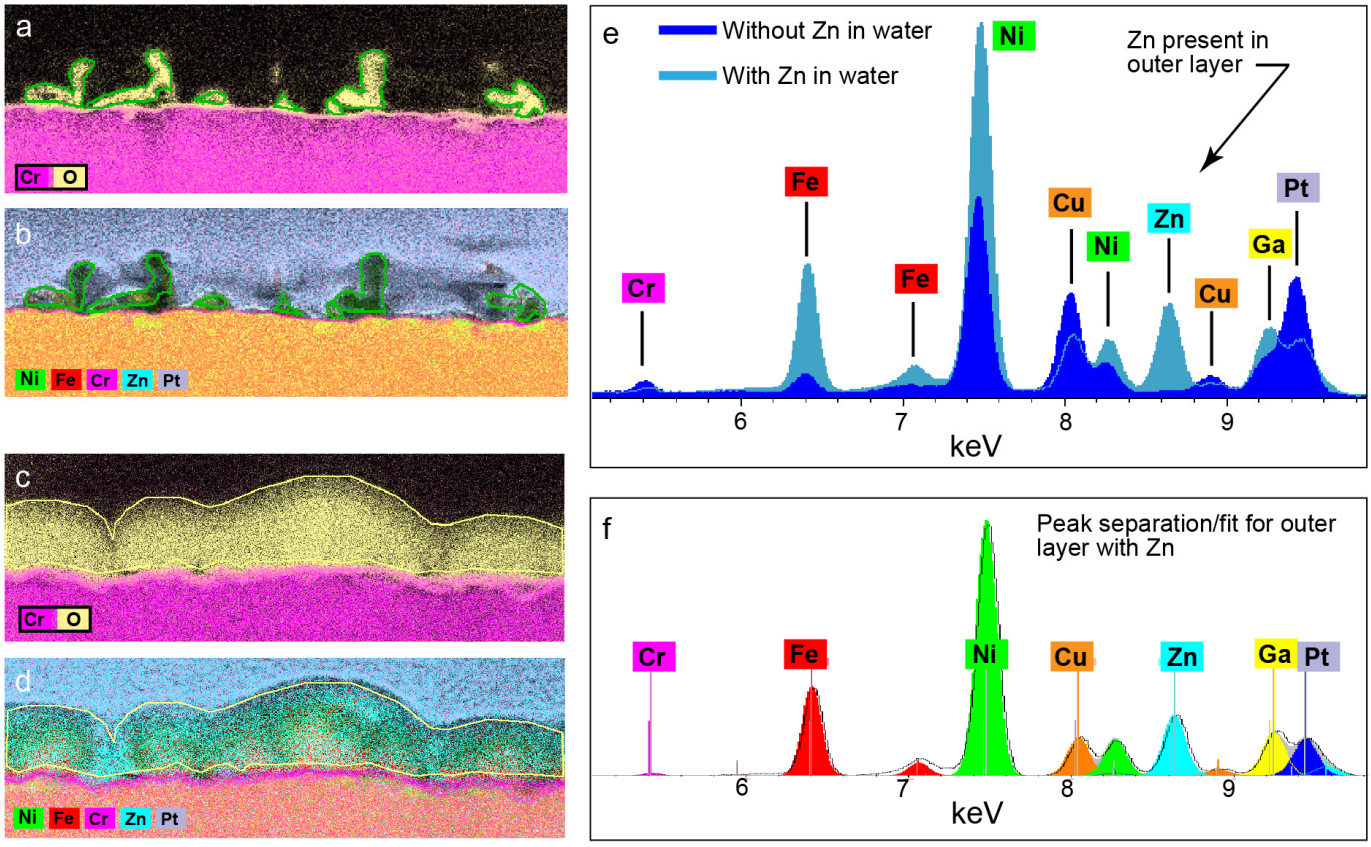

Figure 3. Quantification of the outer layer. (**a**,**b**) EDS maps from the no-Zn sample at −565 mV. The outer-layer oxide whiskers are outlined in green. Spectra from these outlined pixels were summed to generate a spectrum from the outer layer that had sufficient signal to noise to fit the spectral peaks and quantify the atomic percent of elements using the Cliff–Lorimar ratio method (41). The spectrum from these pixels is shown in dark blue in (**e**) in which it can be seen that there is no peak from Zn. (**c**,**d**) EDS maps from with-Zn sample at −550 mV. The more continuous outer layer is outlined in yellow. Spectra from the outer-layer pixels were summed to generate the spectrum shown in turquoise in (**e**) where the peak corresponding to the Zn is present. (**f**) The summed spectrum from the with-Zn sample after background subtraction and peak separation. A similar analysis was conducted to quantify the Cr-rich inner layer and the substrate; those results are shown in Table S1.

Table 1. Mean atomic percent in OL of Alloy 600 in PWR PW with no zinc.

Potential	Oxygen	Chromium	Iron	Nickel
−695 mV	57.0	2.2	7.6	33.3
−565 mV	59.5	2.0	3.4	35.1
−223 mV	53.4	3.6	8.8	34.1

3.1.3. Outer Layer—TEM Results for PWR PW with 100 ppb of Zinc

ADF-STEM images and linescans from each of the three TEM cross-sections of samples polarized in zinc-containing PWR PW at −690 mV, −570 mV, and −223 mV are presented in Figures 4, S3 and S4, respectively. The STEM images show a dense OL covering the IL at all three potentials, which was in agreement with the SEM micrographs in Figure 1d–f.

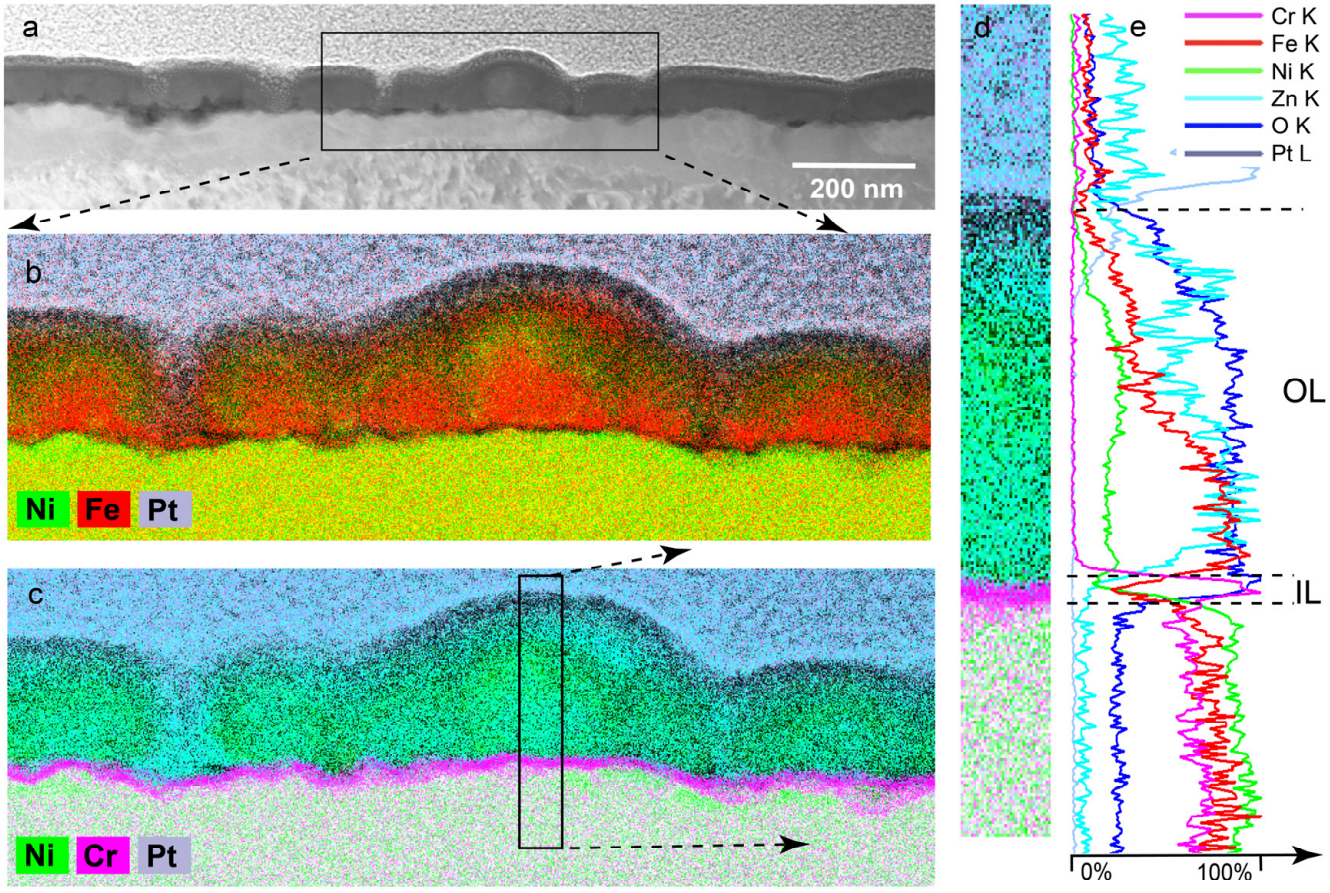

Figure 4. (**a**) Dark-field cross-sectional image of Alloy 600 polarized at −570 mV in PWR PW with 100 ppb of zinc. (**b**) EDS map of nickel, iron, and platinum. (**c**) EDS map of nickel, chromium, and platinum. (**d**) EDS map of region of narrow width pictured in (**c**). (**e**) Integrated intensities of elements in region of narrow width plotted on a scale of 0% to 100% for each element's total X-ray count.

The STEM image indicated that the OL formed in the zinc-containing electrolyte at −690 mV was composed of large oxide particles (up to 200 nm) that were often in intimate contact with adjacent particles. There were also a few gaps in the OL in which the IL appeared to be covered by only a very thin OL and possibly was in direct contact with the electrolyte. At −570 mV, the OL was dense and compact and ≈70 nm thick. At −223 mV, the OL was much thinner (≈ 30 nm thick) with some local sites of larger thickness of 100 nm. The linescans presented in Figures 4e, S3e and S4e provide qualitative information about the compositions of the OLs. At all three potentials, the OLs contained nickel, zinc, and iron.

The quantitative compositions of the OLs at all three potentials are summarized in Table 2 (the detailed results are presented in Table S3). The OLs contained significant amounts of zinc and approximately half the amounts of nickel and iron found in the OLs formed in the zinc-free solution.

Table 2. Mean atomic percent in OL of Alloy 600 in PWR PW with 100 ppb of zinc.

Potential	Oxygen	Chromium	Iron	Nickel	Zinc
−690 mV	60.7	1.1	4.3	19.0	14.9
−570 mV	73.5	0.1	4.5	15.3	6.5
−223 mV	58.3	4.9	6.3	19.1	11.3

In summary, in both the zinc-free and zinc-containing electrolytes, the OL and the whiskers were an oxide predominantly with Ni and some Fe. The zinc was measured to be 6–15 atomic % in the outer layer of the samples exposed to Zn containing water; no zinc was detected in the samples that were exposed to water that did not contain Zn. While a small amount of Cr was detected using EDS, it is unknown whether this was due to delocalization of the Cr signal from the IL or if it was actually present.

3.1.4. Inner Layer

The inner layers of all six samples were thin (between 6 nm and 20 nm in thickness), and the interface between the inner layer and the alloy was irregular in shape and suggested an uneven growth of the inner layer into the alloy.

The inner layer was enriched in chromium and was associated with chromium-depleted zones in the alloy immediately underneath the IL. The chromium-depleted zones were discontinuous along the interface. The chromium enrichment is readily shown in the EDS maps in magenta, and the change in the Cr X-ray signal as a function of depth in the layer is shown in the corresponding line scan (Figures 2c,e and 4c,e).

The thickness and composition of the Cr-rich IL were the same in both the zinc-free and zinc-containing solutions. There was no significant evidence of zinc in the chromium-rich inner layer (IL). However, given the uncertain precision of our EDS measurements, we could not completely rule out the presence of a small amount of zinc. That is, the most we can state with confidence is that the zinc concentration was less than 1% in the IL.

The nickel concentration of the inner layer was also uncertain. At 200 kV and with the amount of incident beam current, we estimated that the size of the focused probe was on the order of 1–2 nm. Due to the thickness of the TEM samples (≈70 nm to 120 nm), there was significant spreading of the incident and scattered electrons, which led to an excited volume that was of a significant size relative to the thin IL. The combination of beam broadening and a thin IL made it difficult to specify the nickel concentration of the IL, although Ni X-rays were detected when the focused probe illuminated the IL. This was visualized by examining the green linescan from the Ni X-ray counts, in which it can be seen that the Ni signal dropped from a high value in the substrate to a lower value in the outer layer. That the IL likely contained some amount of nickel was suggested by the high concentration of nickel in the OL.

In a separate investigation conducted in our laboratory (using the same autoclave and high-temperature/high-pressure water loop, the same source of Alloy 600, and the same electrolyte composition), in situ surface enhanced Raman spectroscopy (SERS) indicated the IL of Alloy 600 in zinc-free PWR PW was very nearly identical to chromium's surface film, which SERS indicated was either Cr_2O_3 or CrOOH (Cr_2O_3 and CrOOH have similar Raman spectra.) [42–45]. Our finding of a chromium-rich IL of Cr_2O_3 or CrOOH was in agreement with results of Voyshnis et al. [35], who used ToF-SIMS to identify the IL at 1 h of immersion as Cr_2O_3.

In summary, the main results of SEM and STEM/EDS were:

1. Surface films of Alloy 600 in PWR PW with and without 100 ppb of zinc were duplex structures with a chromium-rich inner layer (IL) and a nickel-rich outer layer (OL).
2. The thickness (≈6–20 nm) and composition of the chromium-rich IL were the same in both the zinc-free and zinc-containing solutions.

3. The IL was Cr-rich and presumed to be Cr_2O_3 and/or CrOOH; and narrow, discontinuous chromium-depleted zones were in the alloy beneath the IL (evident as green nickel-rich regions in the alloy substrate).
4. The structures and compositions of the OL were very different for the zinc-containing and zinc-free PWR PW.
    a. In the zinc-free electrolyte at potentials of −695 mV and −565 mV, the OL was mostly composed of nickel-rich oxide whiskers with relatively small concentrations of iron and very small concentrations of chromium. The whiskers were structurally equivalent to a highly porous or discontinuous layer. At an applied potential of −223 mV, the OL was nearly free of whiskers.
    b. In the zinc-containing electrolyte, there were no whiskers and the OL contained a significant amount of zinc and had only half the amounts of nickel and iron found in the whiskers, which formed the OL in zinc-free PWR PW. The OL formed in the zinc-containing PWR PW was relatively thick and compact and provided near-continuous coverage of the IL.
5. Thus, zinc's main effect was to alter the composition and the structure of the OLs formed at ≈ −700 mV and ≈ −550 mV.

3.2. Potentiodynamic Polarization Tests

The potentiodynamic cathodic and anodic polarization curves of Alloy 600 in PWR PW with and without zinc ions are presented in Figure 5. The cathodic polarization curves in the zinc-free electrolyte were identical to those in the zinc-containing electrolyte, which indicated that zinc had no effect on the kinetics of the hydrogen reduction reaction. At potentials from ≈ −600 mV to 0 mV, the rate of oxidation in the zinc solution was lower than that in the zinc-free solution by a factor of approximately 1.5. Given (1) the small difference in oxidation rates and (2) that current densities measured in the potentiodynamic polarization tests were not steady-state values, potentiostatic polarization tests were conducted to more rigorously assess the influence of zinc on the oxidation rate of Alloy 600.

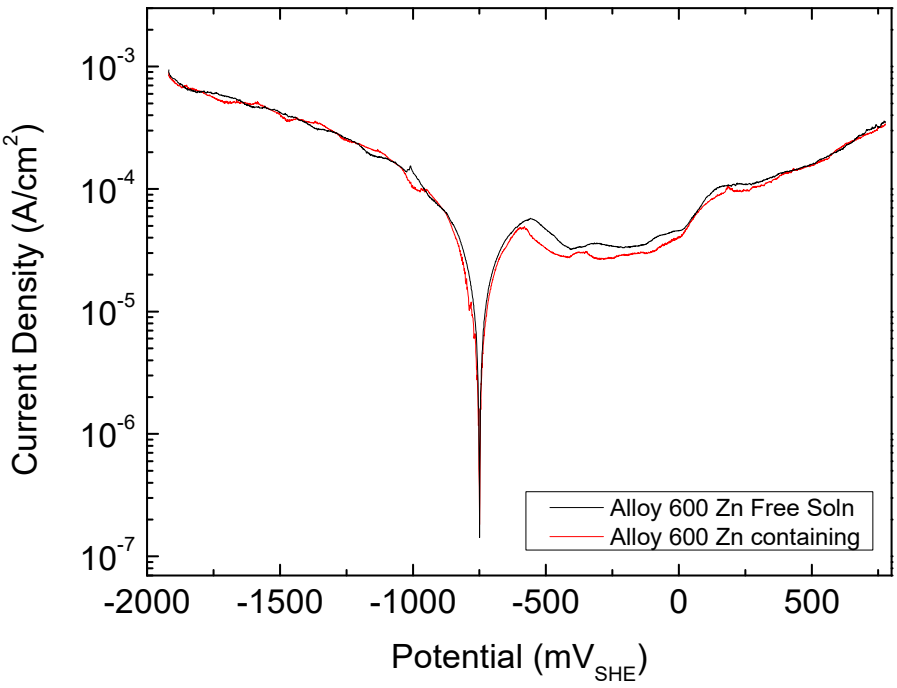

Figure 5. Potentiodynamic polarization curves of Alloy 600 in PWR PW at 320 °C with and without 100 ppb of zinc.

3.3. Potentiostatic Polarization Tests

The lower rate of oxidation in the zinc solution was confirmed via potentiostatic tests. A total of 54 potentiostatic tests were conducted. Three tests were conducted in each electrolyte (with and without Zn) at nine different potentials from −743 mV to −223 mV. The wide range of potentials included the relatively large range of values of corrosion potential that Alloy 600 exhibits in PWRs due to different applications with different dissolved oxygen concentrations and variations in the dissolved oxygen concentration from start-up to steady-state operation [1,4]. For example, after shutdown the primary water adjacent to CRD tubes is air-saturated (≈9 ppm), and concentration can reach 1350 ppm after pressurization at 343 °C. Another example is the air-saturated water that is added during load-following. Air saturation can create corrosion potentials at 325 °C in PWR PW that are above 0 mV. The wide range of potentials was also investigated to reveal trends with potential that might help to identify the mechanism(s) of oxidation.

The cell currents reached a quasi-steady state in less than four hours. The values of the cell currents at four hours of immersion are presented in Figure 6. At potentials between −673 mV and −523 mV, the cell current was anodic and the average value of the anodic cell current in zinc-containing solution was consistently lower than in zinc-free solution; however, as was the case for the potentiodynamic polarization tests, the difference was not great. The difference between the oxidation rate in the zinc-free and zinc-containing electrolytes increased with an increasing potential starting at −423 mV.

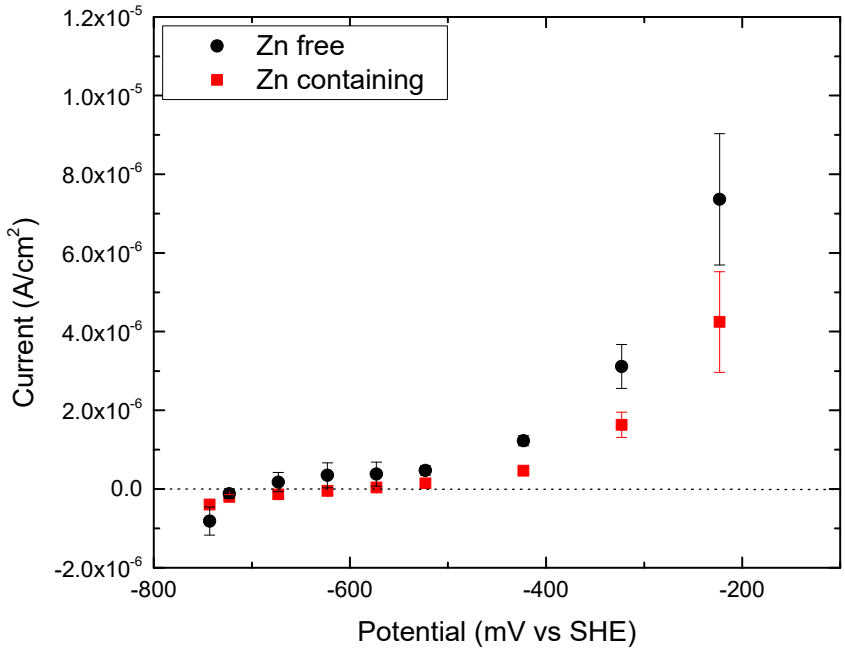

Figure 6. Influence of potential on the steady-state cell current density of Alloy 600 potentiostatically polarized in PWR PW at 320 °C with and without 100 ppb zinc.

In summary, the results of the potentiostatic polarization tests indicated that aqueous zinc ions lowered the oxidation rate of Alloy 600 during immersion times of up to four hours, albeit by a small amount. Thus, zinc lowered the corrosion rate after 4 h of immersion just as it lowered the corrosion rate of A600 tubing following hundreds to thousands of hours of in-reactor service [3,8,9]. The zinc effect following hundreds to thousands of hours of in-reactor service was greater than after 4 h of immersion in our lab-simulated PWR PW [3,8,9], which indicated that our study was in the early stages of corrosion.

EIS can provide information about both oxidation and reduction reactions. Accordingly, based on the results of the polarization tests, EIS was conducted at specific potentials between −773 mV and −223 mV in both the zinc-free and zinc-containing electrolytes in order to identify the step in the corrosion process where Zn had the largest effect.

3.4. Electrochemical Impedance Spectroscopy

3.4.1. Introduction

The EIS was conducted in two different testing conditions. Each testing condition consisted of several steps, which were described in the Materials and Methods section. The motivation for employing two testing conditions was as follows.

First Set of Testing Conditions. The EIS of the samples, which were later examined by SEM and TEM, was conducted at potentials of ≈−700 mV and ≈−550 mV. Each test was preceded by 48 h in an open circuit followed by 4 h of polarization at the test potential. The four hours of polarization allowed the sample to reach a steady state before starting the EIS measurements. Each EIS measurement took approximately 3 h. Multiple measurements exhibited scatter of ±250 ohms·cm^2 at high frequencies. In the Bode plots, the scatter at frequencies above 100 Hz was readily apparent. The scatter was attributed to test-to-test variations in the relative positions of the three electrodes (WE, CE, and RE).

Generally, scatter at frequencies above 100 Hz is of minor importance because, as just stated, the impedance at high frequencies is attributed to the ohmic resistance of the cell. The impedance at frequencies below 100 Hz contains information about the electrochemical reactions and ion transport through the surface film. Nevertheless, as described below, the high-frequency impedance did indicate the presence/absence of whiskers. The information about whiskers was captured by using a second set of testing conditions.

Second Set of Testing Conditions. The first set of testing conditions indicated a significant difference in the EIS data at ≈−700 mV and ≈−550 mV. To comprehensively investigate the influence of potential, EIS was conducted on a single sample at nine different values of potential. The first EIS was conducted at −743 mV. Next, the potential was stepped +50 mV to −693 mV and held for four hours before conducting the EIS. The procedure was repeated in +50 mV increments to a final value of −223 mV. Since the tests were conducted on a single sample, the interelectrode spacings were the same for all tests, so there was no effect of variable interelectrode spacing on the impedance at frequencies greater than 100 Hz. Any changes with potential to the impedance at frequencies above 100 Hz were attributed to changes that occurred in the immediate vicinity of the WE of Alloy 600; e.g., the formation/removal of whiskers.

Importantly, the EIS data at a potential of ≈−700 mV using the first set of test conditions were the same as the EIS data measured at ≈−700 mV using the second set of test conditions. The same was true for the EIS data measured at ≈−550 mV. That is, the EIS data were strongly dependent on the potential of the measurement but practically independent of the history of the potential prior to the testing potential. Consequently, we used the 50 mV increments to develop equivalent circuits (ECs) as functions of potential. We used the SEM/TEM to assign the components of the ECs to specific electrochemical reactions and aspects of the surface films. The validity of our approach was confirmed by the excellent fit of the EIS of the SEM/TEM samples that were subjected to the first set of test conditions to the ECs derived from the EIS conducted at the nine values of potential separated by 50 mV.

3.4.2. Overview of EIS Results

The EIS data as a function of potential were determined by the second set of test conditions. The results are presented as Nyquist plots in Figures 7 and 8.

Collectively, the spectra at the nine values of potential clustered into three groups in which the spectra in each group exhibited a similar shape. The first was composed of spectra at −743 mV and −723 mV and was named Group 700. The second group consisted of spectra at potentials of −673 mV through −523 mV and was called Group 550. The third and final group contained spectra at −423 mV to −223 mV and was referred to as Group 223.

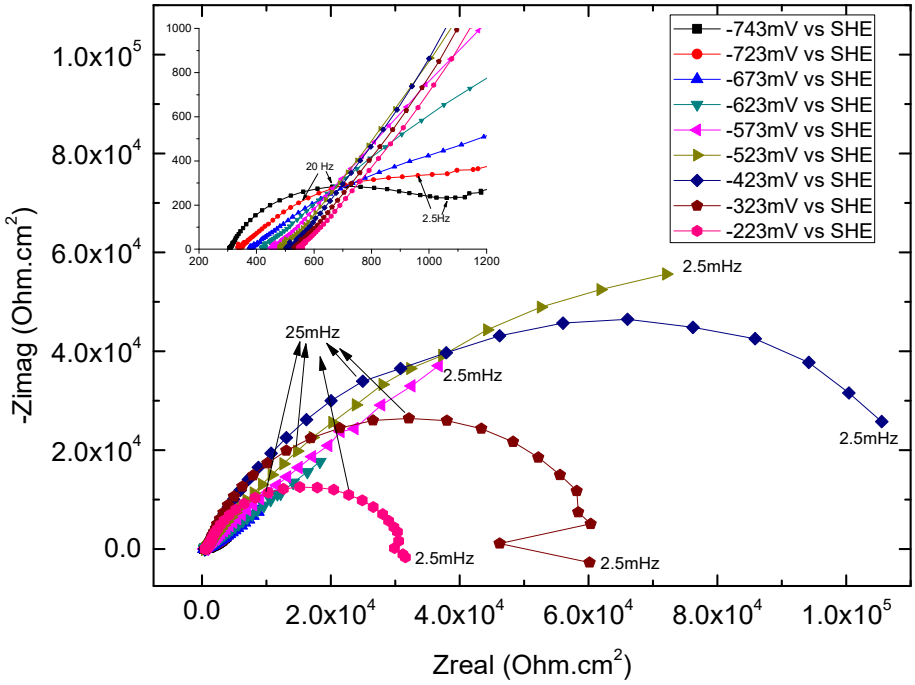

Figure 7. Nyquist plots of Alloy 600 in PWR PW (no zinc) at 320 °C as a function of potential.

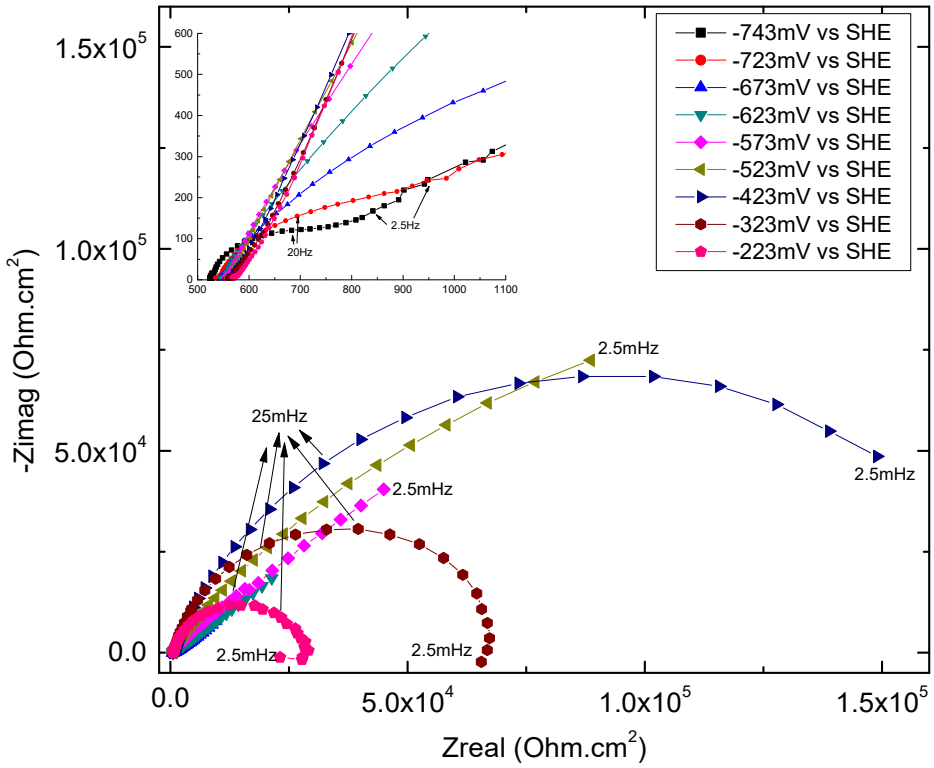

Figure 8. Nyquist plots of Alloy 600 in PWR PW with 100 ppb of zinc at 320 °C as a function of potential.

The next step was the analyses of the EIS. To facilitate the analysis of the effect of aqueous zinc, the results were subdivided into (1) the high-frequency impedance (frequency > 100 Hz), which was dominated by current flow in the electrolyte; and (2) the low-frequency impedance (frequency < 100 Hz), which was dominated by the electrochemical reactions and transport of ions through the surface film.

3.4.3. High-Frequency Impedance of Groups 700, 550, and 223

The effect of zinc on the high-frequency impedance provided key information about how zinc lowered the oxidation rate of Alloy 600. The effect of zinc on the high-frequency impedance is shown in the plots of log impedance modulus vs. log frequency (Figure 9 (no Zn) and Figure 10 (Zn)). In these spectra, the log of the impedance modulus was analogous to plotting the log of the real component. Indeed, the plots of log real Component for the Zn tests and no-Zn tests that are presented as Figures S5 and S6 are similar to the plots of the log modulus in Figures 9 and 10.

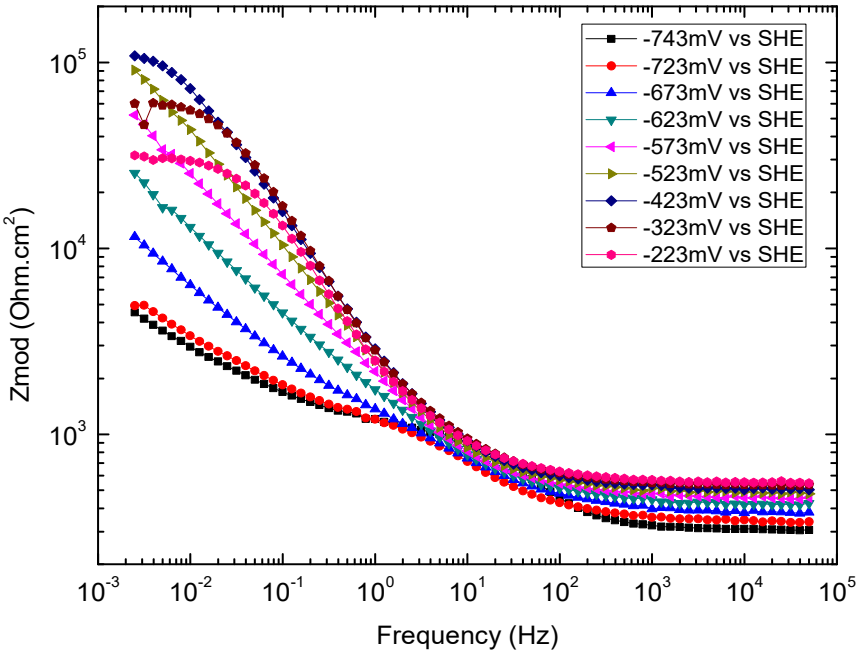

Figure 9. Log impedance modulus vs. log frequency of Alloy 600 in PWR PW (no zinc) as a function of potential.

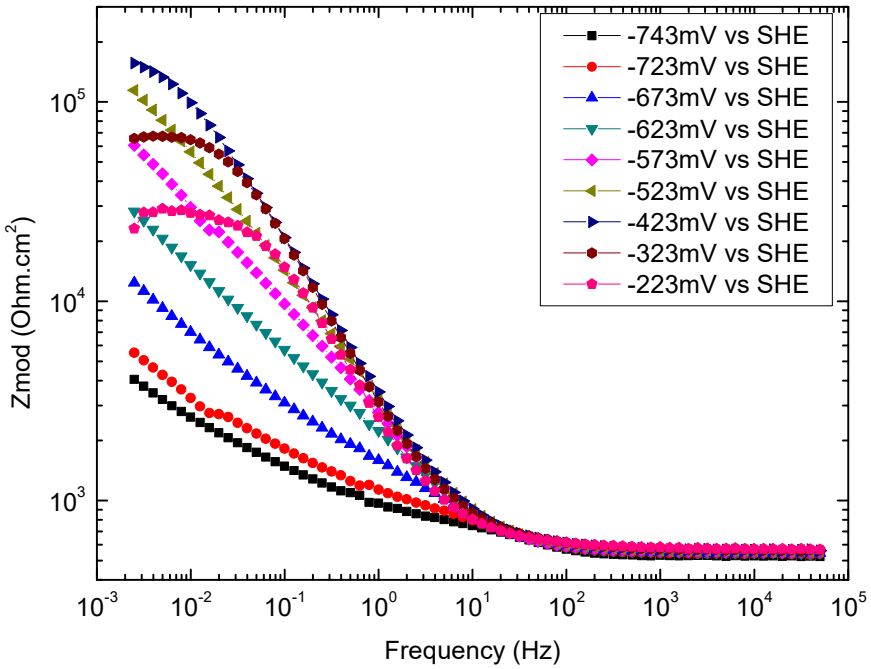

Figure 10. Log impedance modulus vs. log frequency of Alloy 600 in PWR PW with 100 ppb of zinc as a function of potential.

The influence of the potential on the high-frequency modulus is summarized in Figure 11. At high frequencies, the real component (and modulus) of the Zn test at −743 mV was approximately twice that of the no-Zn-test. As the applied potential became more positive, the high-frequency real component (and modulus) of the Zn test remained constant and that of the no-Zn test continuously increased until both values were equal at potentials of ≥≈−423 mV.

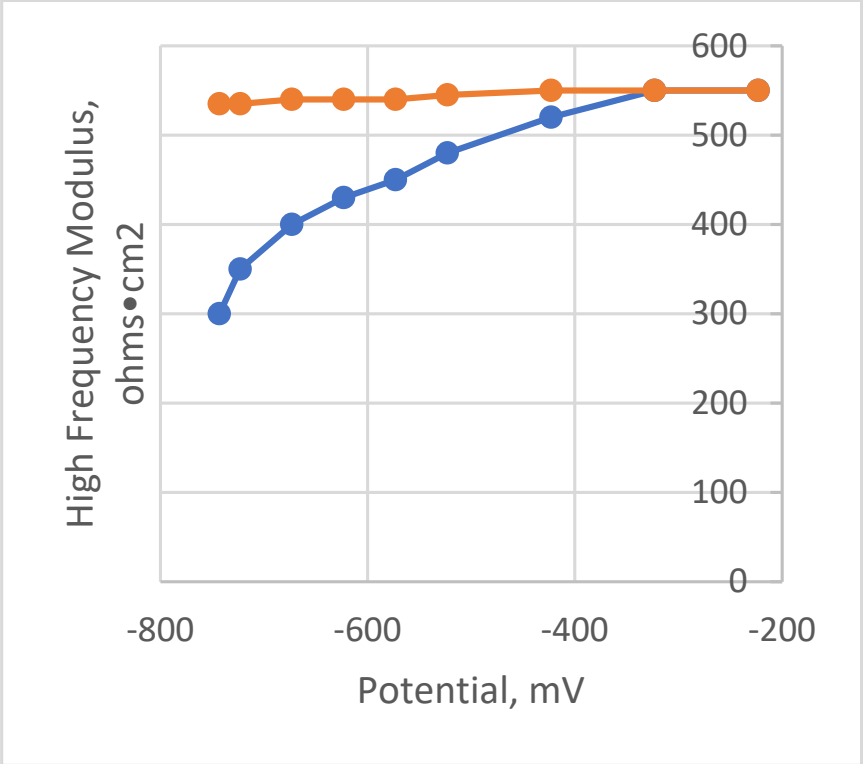

Figure 11. Influence of DC potential on the high-frequency modulus (ohm·cm^2) for tests conducted in PWR PW without zinc (blue curve). For the tests in PWR PW with 100 ppb of zinc (red curve) the modulus is a constant with potential and is equal to Rs = 550 ohm·cm^2.

Potential-dependent changes also occurred in the plots of log imaginary component vs. the log frequency at high frequencies (see Figures S7 and S8 in the Supplementary Materials); however, the magnitude of the imaginary component was approximately 50X smaller than the magnitude of the real component, so the potential dependent changes in the modulus were the result of changes in the real component.

The TEM/SEM results, which were presented in the preceding section, suggested an explanation of the differences in the high frequency real component of the EIS. In tests with and without zinc, the samples of Alloy 600 formed ILs that were similar in thickness, structure, and composition. However, their OLs were quite different. The most distinguishing features of the SEM images in Figures 1a–c and 2a–c were the potential-dependent presence of nickel oxide whiskers (NOW) on the surfaces of the no-zinc samples and the complete absence of NOW on the with-zinc samples. As described by Orazem and Tribollet, the impedance of the porous outer layer can be represented by a parallel arrangement of a resistor and constant phase element that are in series with the electrolyte's ohmic impedance and the faradaic impedance of the sample [46]. The capacitance (CPE) of the porous outer layer was very small, so the characteristic frequency of the R-CPE couple was much higher than the frequency range of our impedance equipment. As a result, the only detectable effect of the porous outer layer at high frequencies was on the real component. We concluded that the porous NOW in the OL was the cause of the potential dependance of the blue curve shown in Figure 11.

In summary, the relatively high value of the real component in the sample exposed to the Zn-containing water was constant with the potential. The potential independency was attributed to a mostly compact OL and the complete absence of NOW. The potential dependency of the real component of the no-Zn tests correlated with the presence of NOW and with their disappearance at more positive potentials and their replacement by an OL that had less porosity, which was similar to that of Zn test samples.

3.4.4. Low-Frequency Impedance of Groups 700, 550, and 223

The analyses of the low-frequency impedance yielded an equivalent circuit (EC) for each of the three groups. For each group, the EC representing the low-frequency impedance was composed of the same electrical components for both zinc and no-zinc. Zinc's effect was on the magnitudes of particular electrical components of the ECs. Deriving the ECs for the low-frequency impedance required detailed analyses of the EIS, which are presented in the Supplementary Materials.

The differences in the numerical values of particular components of the ECs caused by zinc are described in the Discussion section.

Group 700. The magnitude and polarity of the potentiostatic current densities (Figure 6) suggested that both oxidation and reduction reactions contributed to the impedances measured at −743 mV and −723 mV. These two potentials are cathodic, so the impedance was dominated by the reduction reaction (see Appendix A, Section A.1 and Section A.2.1). As discussed in Appendix A (Section A.2.1.1, Section A.2.1.2, Section A.2.1.3, Section A.2.1.4, Section A.2.1.5), the low-frequency EIS at potentials of −743 mV and −723 mV suggested the equivalent circuit (EC) presented in Figure 12 for the EIS in zinc-free and in zinc-containing solution. The excellent fit of the EC to the measured EIS is indicated in the Bode plot presented in Figure 13. The Bode plots included a plot of the phase angle versus the frequency, which provided a very sensitive demonstration of the quality of the fit between the measured impedance and the impedance of the EC.

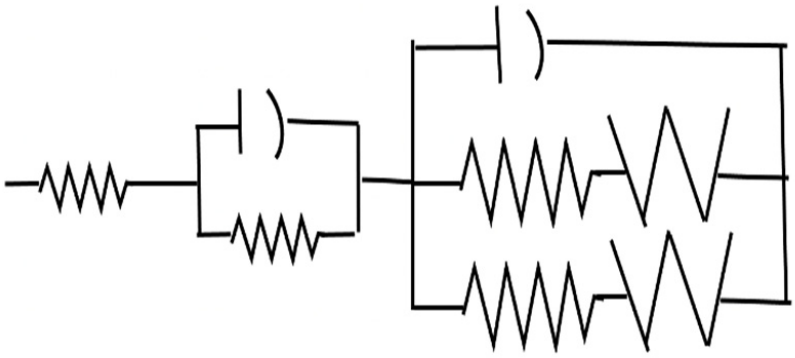

Figure 12. Equivalent circuit of Alloy 600 at −743 mV and −723 mV in Zn-free PWR PW and in PWR PW +100 ppb of Zn at 320 °C.

The EIS at −695 mV in Zn-free electrolyte (first set of testing conditions (FSTC)) and the EIS at −690 mV in Zn-containing electrolyte (FSTC) also exhibited excellent fits to the EC in Figure 12. The results are presented in the Supplementary Materials as Figures S9 and S10, respectively. After the EIS, these two samples' surface films were investigated via SEM and TEM (the results are presented in Section 3.1).

That the EC (Figure A2 in Appendix A) that described the Faradaic reactions and the transport of ions was the same for both the Zn-free test and the Zn-containing test, as well as the fact that the values of the individual components of the ECs were very similar for the zinc-free and zinc-containing tests, indicated that the zinc had no effect on the kinetics and mechanism of the hydrogen reduction reaction. Consequently, zinc's lowering of the corrosion rate was a consequence of zinc's effect on the oxidation of Alloy 600.

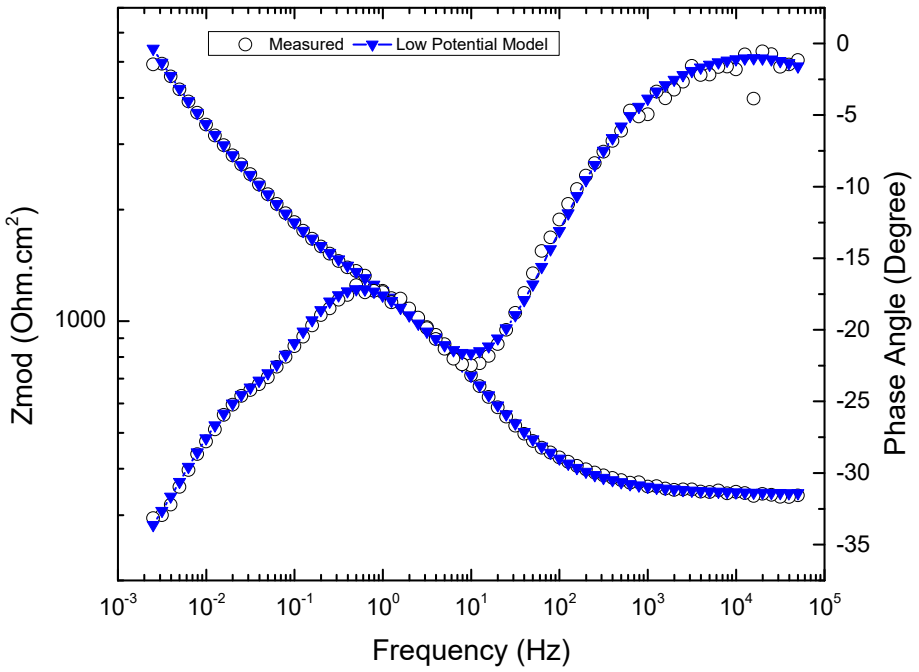

Figure 13. Fitting of the modulus and phase angle of the impedance of EC presented in Figure 12 with the impedance spectrum measured at −723 mV.

Group 550: As discussed in Section A.2.2 of the Appendix A, the EIS data measured at potentials of −623 mV and–573 mV in the zinc-free solution and the zinc-containing solution suggested the EC presented in Figure 14. The influence of the potential and frequency on the impedance are discussed in Section A.2.2.2, Section A.2.2.3, Section A.2.2.4 of the Appendix A. The dependencies on the potential and frequency suggested preliminary assignments of specific electrochemical reactions and transport phenomena to the individual components of the EC. In Section 4 of this paper, more specific and more complete assignments will be made based on the results of the SEM, the TEM/EDS, and comparisons of the zinc and zinc-free results.

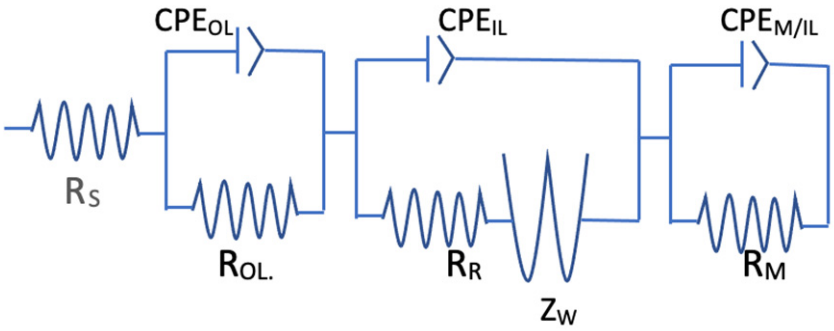

Figure 14. EC of EIS of Alloy 600 at −623 mV and −573 in PWR PW both with and without Zn.

The EC for the impedance at −623 mV and −573 mV was the same as that at −743 mV and −723 mV except for the absence of a second serial arrangement of a resistor (R) and a Warburg impedance (W), which appeared in the EC for −743 mV and −723 mV and were assigned to the electrochemical reduction reaction. That is, the electrochemical reduction reaction did not contribute to the impedance at −623 mV and −573 mV, which made sense given that the equilibrium potential of the hydrogen reduction reaction was −723 mV. The high quality of the fit of the EC (Figure 14) to the measured EIS at −573 mV without zinc is demonstrated by the Bode plot in Figure 15. The EC of Figure 14 provided an equally good fit to the EIS at −573 mV in PWR PW with zinc.

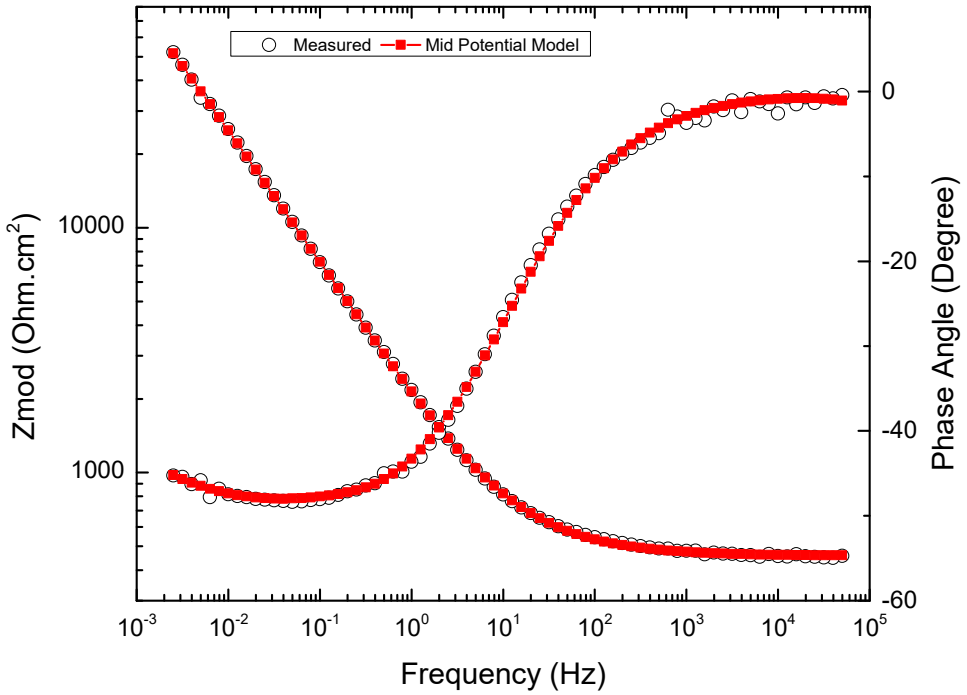

Figure 15. Fitting the modulus and phase angle of the impedance of the EC to the measured impedance at −573.

The EIS at −565 mV in the Zn-free electrolyte (FSTC) and the EIS at −550 mV in the Zn-containing electrolyte (FSTC) also exhibited excellent fits to the EC in Figure 15. The results are presented in the Supplementary Materials as Figures S11 and S12, respectively. After the EIS, these two sample's surface films were investigated via SEM and TEM (the results are presented in Section 3.1).

It was notable that the portions of the ECs that characterized the low-frequency impedance at −623 mV and −573 mV were the same for both the zinc-free and the zinc-containing solutions. However, importantly (and as considered in the Discussion section), the numerical values of the individual circuit components depended on the presence or absence of aqueous zinc ions.

Group 223: The EC that resulted from our analyses of the EIS data at potentials of −323 mV and −223 mV is presented in Figure 16; it was the same for both conditions (with and without Zn PW). Figure 17 demonstrates the high quality of the fit of the EC to the measured EIS.

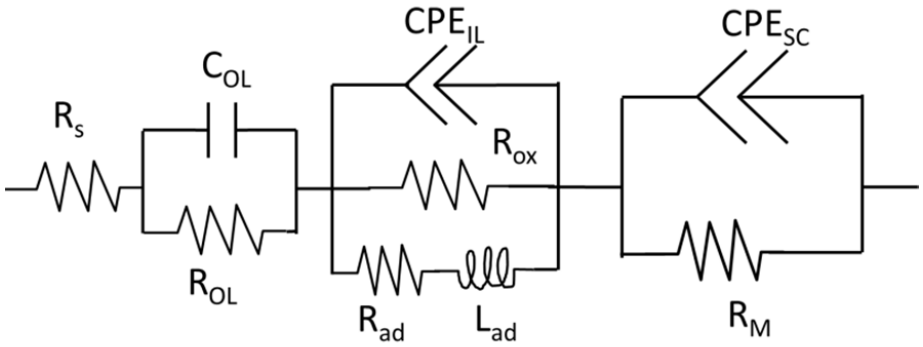

Figure 16. EC for potentials between −500 mV and −200 mV.

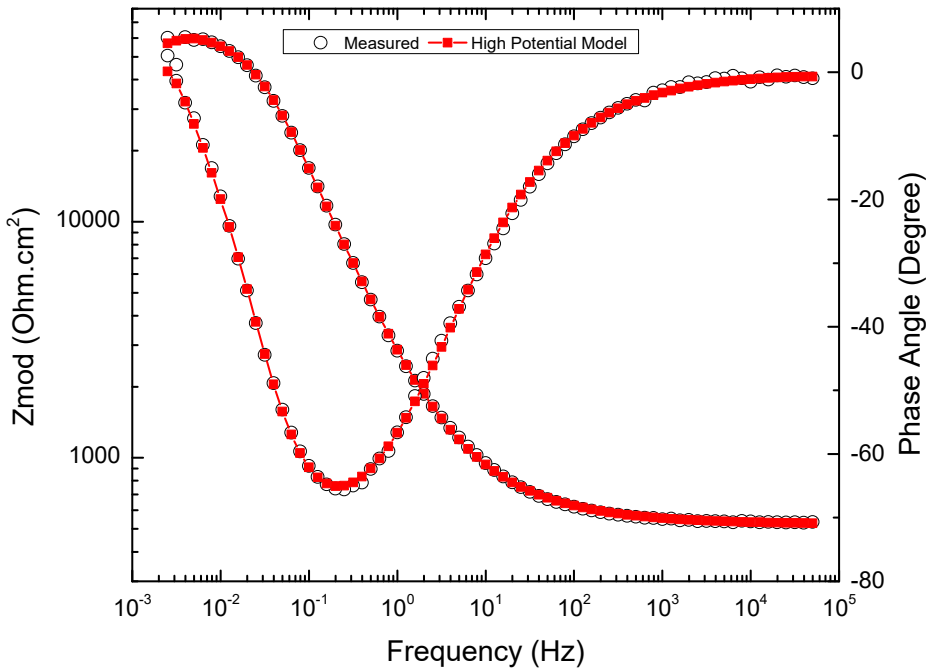

Figure 17. Fitting the modulus and phase angle of the impedance of the EC to the measured impedance at −223 mV.

4. Discussion

The individual components of the ECs were assigned to specific electrochemical reactions, transport phenomena, and features of the surface films. The assignments were based on (1) potential dependencies of the values of the components; (2) the influence of zinc on the values of the components; and (3) the SEM and TEM/EDS results. The influence of the potential and zinc on the values of the components of the EC are summarized in Figures 11, 18a–c and S13a–c, as well as Figures 19 and 20 below.

The following analysis indicated that the dense outer layer formed in the zinc-containing PWR PW and the porous outer layer formed at relatively low potentials in the zinc-free PWR PW had different effects on the low-frequency impedance, which helped to clarify the influence of zinc on the corrosion rate of Alloy 600.

Low-Frequency Impedance

The EC presented in Figure 14 indicates that the resistive impedance of the oxidation reaction was composed of two resistances (R_m and R_R)) and a Warburg impedance (Z_W) in series. Thus, it was interesting to note that our EC, which was developed via graphical analyses, possessed the same components for the multistep oxidation reaction of Alloy 600 as did the kinetic analyses of Yang et al. [32] and Bojinov et al. [38]. To determine the nature of zinc's effect on the oxidation of Alloy 600, we first considered which steps of the multistep oxidation of Alloy 600 were associated with Rm and R_R. Then, we considered the effects of zinc on each of the resistive elements and the Warburg impedance.

The shape of the Nyquist plots (Figures 7 and 8) at −673 mV and −623 mV at low frequencies (i.e., straight lines with positive slopes of +0.84) and the shapes of the Bode plots at low frequencies (i.e., straight-line plots of log im. and log re. vs. log frequency with slopes −0.46 and −0.41, respectively, and the phase angle that was approximately constant at 45–48° over three decades of frequency (Figure 15)) indicated that the dominant impedance of oxidation of Alloy 600 at 4 h of immersion was Z_W; i.e., diffusion. Previous studies reported that diffusion was also the dominant impedance after thousands of hours of immersion [4,9].

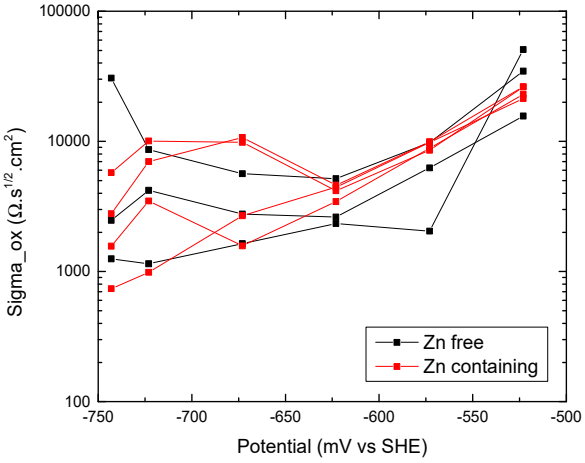

(**a**)

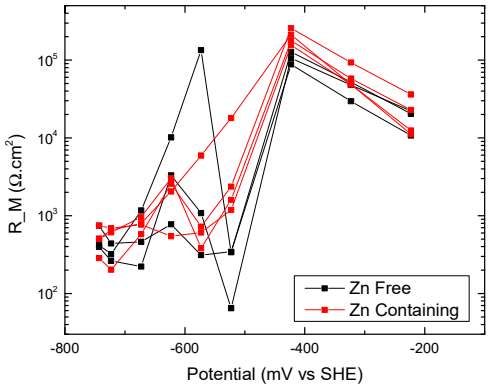

(**b**)

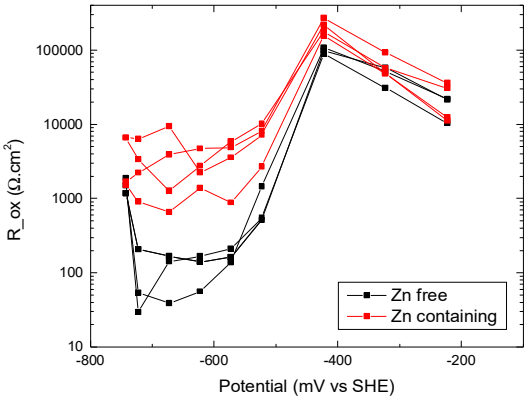

(**c**)

Figure 18. The influence of the potential on the values of those critical circuit elements that identified the influence of aqueous zinc ions on the corrosion rate of Alloy 600 in PWR PW at 320 °C. (**a**) Warburg coefficient associated with diffusion of ions in the IL. (**b**) Resistance associated with oxidation of metals at the metal/IL interface. (**c**) Resistance attributed to cation release from IL.

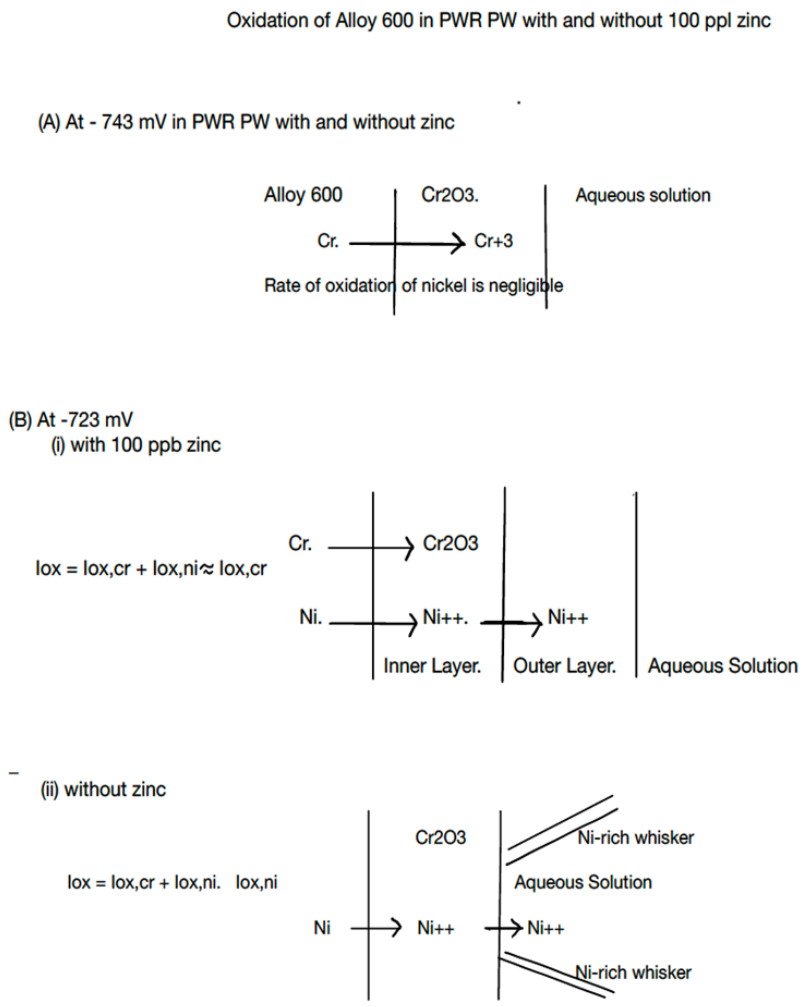

Figure 19. Schematic of the oxidation reactions of Alloy 600 as a function of potential in PWR PW with and without 100 ppb of zinc.

Results of an earlier study showed that after hundreds to thousands of hours of immersion, zinc lowered Alloy 600's oxidation rate by decreasing the rate of ion (e.g., Ni^{++}) diffusion through the IL (4). In contrast, in our work, the plots (Figure 18a) of sigma vs. potential (σ is the Warburg coefficient of the Warburg impedance ($Z_W = \sigma\omega^{-1/2}$) associated with ion diffusion in the IL; $\sigma \sim D^{-1/2}$) in PWR PW with and without zinc indicated that after 4 h of immersion, the presence of Zn did not affect the transport of ions through the IL. We concluded that a factor other than diffusion was responsible for zinc's lowering of the oxidation rate.

The results presented in Figure 18b indicated that at 4 h of immersion, there was no effect of zinc on R_m. Because we found no evidence of zinc in the IL, we assigned R_m to an impedance associated with the IL. Specifically, R_m was assigned to the oxidative charge transfer reaction (i.e., M-> M^{+z} + ze^-) at the alloy/IL interface. Previous reports also found that zinc had no influence on the oxidative charge transfer reaction at the alloy/IL interface for hundreds and thousands of hours of immersion [4,9].

The remaining components of the EC to consider were the capacitive (CPE) elements and R_R. It is unlikely that the capacitive elements could account for zinc's effect on the oxidation rate; a discussion of the capacitive elements is presented in the Supplementary Materials.

By far, the largest effect of Zn was on the value of R_R. As discussed below, R_R was 15 times greater for the Zn test than for the no-Zn test. Accordingly, the focus of the remainder of our discussion is on R_R. In particular, we sought to determine the reaction that was responsible for R_R.

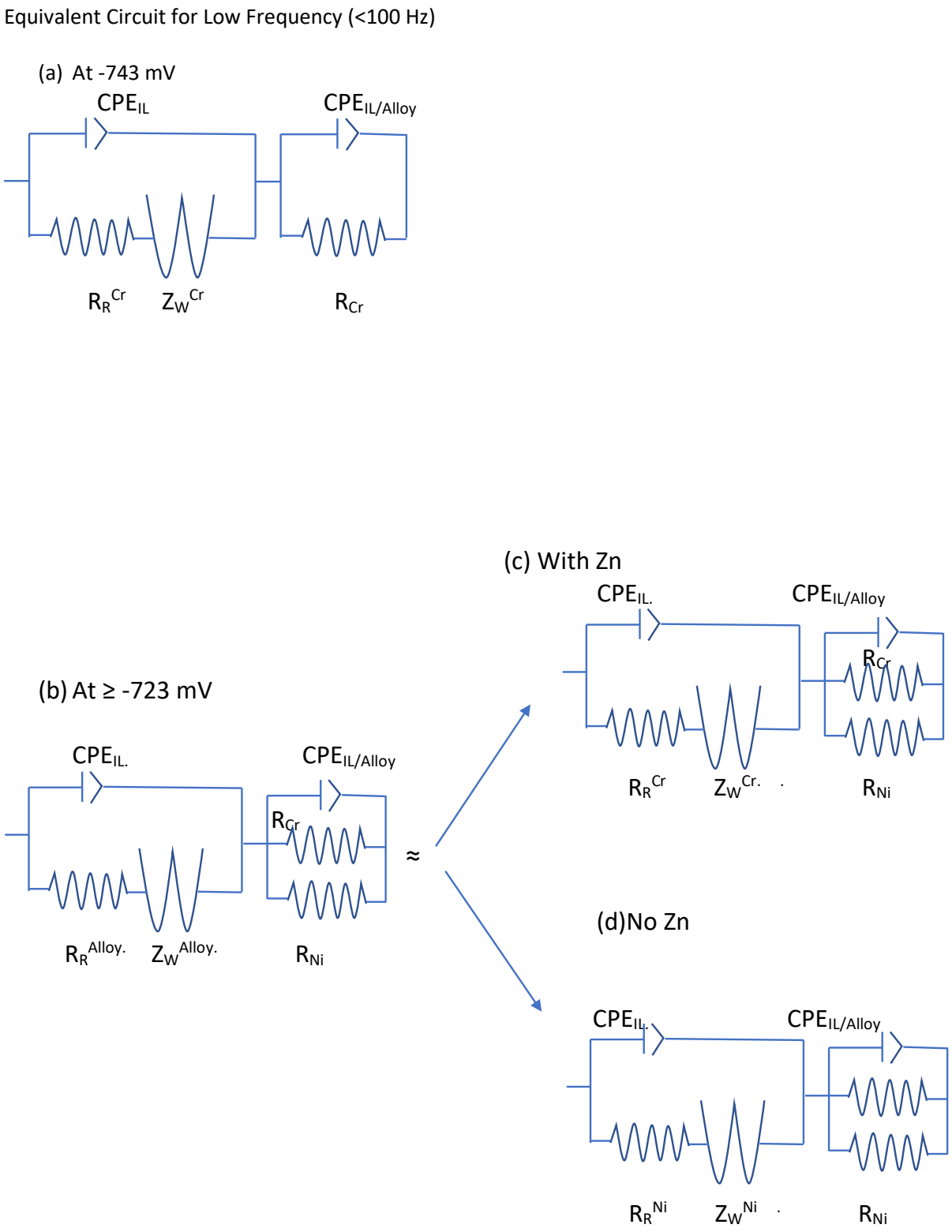

Figure 20. Equivalent circuits representing the impedance at low frequencies of the oxidation of Alloy 600. (**a**) Impedance being measured is Cr alone because potential is too low for Ni oxidation; (**b**) Impedance being measured at -723 mV and above is from both Cr and Ni, however, the measured impedance is dominated by the lower impedance of Ni. There are two cases: (**c**) Ni impedance with Zn; (**d**) Ni impedance without Zn.

As already mentioned, R_R is one part of a three-step oxidation process. The other two steps were discussed above. These two steps are the charge transfer reaction at the metal/IL interface, which is represented by R_m; and ion diffusion through the IL, which is represented by a Warburgh impedance (Z_W). Determination of the reaction associated with R_R is challenging, not just because it is in series with R_m and Z_W, but also because both chromium and nickel contribute to R_R and their relative contributions change with potential.

The potential-dependency of R_R with Zn and without Zn helped to identify the reaction associated with R_R. The findings are summarized in the sketches shown in Figure 19. At −743 mV, $R_R^{(withZn)}$ was equal to $R_R^{(No\text{-}Zn)}$ = 1.5 × 10^3 ohm·cm^2. At −743 mV, both $R_R^{(withZn)}$ and $R_R^{(No\text{-}Zn)}$ were associated with the oxidation of chromium and not nickel. Nickel oxidation was not considered because the equilibrium potential of nickel is −760 mV, which suggested the amount of oxidation of nickel at −743 mV was small (see Figure 19A).

As shown in Figure 18c, as the potential was changed from −743 mV to −723 mV and to potentials up to −573 mV, the value of $R_R^{(withZn)}$ was unchanged, so we assumed that it continued to be associated with the chromium (Figure 19A,B(i)). The thicknesses of the Cr-rich IL of Cr_2O_3 at −743 mV of the Zn test and of the no-Zn-test were equal (≈6–20 nm) and were equal to the thicknesses of the IL of Cr_2O_3 at −623 mV of the Zn test and of the no-Zn-test, which strongly supported the view that R_R was the same at both potentials and in both solutions and, therefore, rightly assigned to $R_{R,Cr}$.

In marked contrast to $R_R^{(withZn)}$, $R_R^{(No\text{-}Zn)}$ decreased by a factor of 15 when the potential was changed from −743 mV to −723 mV, and it remained at that relatively low value as the potential was increased to −673, −623 mV, and −573 mV. While $R_R^{(No\text{-}Zn)}$ at −743 mV was associated with the chromium, $R_R^{(No\text{-}Zn)}$ at potentials more positive than −743 mV was related to nickel.

Given (1) that there was no zinc effect at −743 mV on R_R, (2) that there was a significant zinc effect on R_R at −723 mV and more positive potentials, and (3) that the equilibrium potential of nickel was −760 mV, we hypothesized that in the absence of aqueous zinc ions and at potentials sufficiently more positive than nickel's equilibrium potential, the oxidation reaction that dominated the impedance was the oxidation of nickel (see Figure 19B(ii) and the following paragraph). The Ni^{++} ions were presumed to enter into the Cr-rich IL, diffuse to the outer surface of the IL, and dissolve into the aqueous solution. The $Ni^{++}{}_{aq}$ precipitated out of solution and formed Ni-rich whiskers.

The entire set of reactions that summed together to produce $Ni^{++}{}_{aq}$ was in parallel with the oxidation of Cr, which created the Cr-rich IL (see Figure 19B). Thus, the dramatically lower R_R in the no-Zn test was assigned to $R_{R,Ni}$; that is, oxidation of Alloy 600 was represented by the EC shown in Figure 20a. R_{Cr} was associated with the oxidation of Cr at the alloy/IL interface, and W_{Cr} was assigned to the ion transport ($O^=$ and/or Cr^{+3}) through the IL, which grew the IL. The multistep oxidation of chromium was in parallel with the multistep oxidation of nickel. R_{Ni} was created by the oxidation of Ni at the alloy/IL interface. The nickel ions diffused through the IL and were then transferred out of the IL and into the OL. W_{Ni} was assigned to the ion transport ($O^=$ and/or Ni^{+2}) through the IL. Since the two (oxidation plus transport) processes for nickel and for chromium were in parallel, the net impedance was primarily that with the lower value. Thus, the serial arrangement of R + W in the EC of Figure 14 was assigned to the oxidation of Cr at −743 mV (Figure 20a) and was attributed to the oxidation of Ni at potentials more positive than −743 mV for Zn-free (Figure 20b,d).

The question regarding how zinc decreased the corrosion rate of Alloy 600 has now been converted into a question regarding how zinc increased the value of $R_{R,Ni}$. As already mentioned, the oxidation of nickel was a multistep process, and $R_{R,Ni}$ was the resistive impedance associated with one of the individual steps, which included the charge transfer reaction at the alloy/IL interface ($Ni \rightarrow Ni^{++} + 2e^-$), the ion transport through the IL, and the exit of Ni^{++} at the interfaces of the IL with the aqueous solution and the OL. The STEM/EDS results indicated that zinc had no effect on the IL. Hence, the effect of zinc

must have been associated with the OL. As already mentioned, the OL in zinc-containing PWR PW was thick and provided nearly complete coverage of the IL. Our explanation of the zinc effect was that zinc increased the resistance of the oxidation reaction by increasing R_R (the resistance associated with the exit of nickel ions out of the IL). Thus, zinc's effects were attributed to the effect of zinc on the outer layer (Figure 20b,c).

In other words, for tests in PWR PW with zinc, Ni^{++} leaving the IL was forced to enter the dense OL, which contributed to a relatively high value of $R_{R,\,Ni}{}^{WithZn}$. In the absence of zinc, the outer layer was largely composed of Ni-rich whiskers and a porous, discontinuous layer, so nickel ions exited the inner layer by dissolving directly into the aqueous electrolyte. The dissolution of Ni^{++} out of the IL and into the Zn-free electrolyte contributed to the low value of $R_{R,Ni}{}^{No\text{-}Zn}$.

Finally, other works attributed the decrease in the radiation dose rate to the high zinc concentration of the OL. Zn is the divalent cation with the strongest binding in the tetrahedral sites of spinels, so Zn^{++} inhibits the incorporation of ^{60}Co [4]. Lab data showed that Zn uptake in fresh oxide decreased the corrosion rate and release rates of SS, A600, and A690 after immersions of hundreds of hours to 3.5 months (4). Given the high zinc concentration we found in the OL at 4 h of immersion, it is possible that 100 ppb of Zn would cause a decrease in the radiation dose rate at 4 h of immersion. It is also possible that the lower corrosion rate caused by aqueous zinc would contribute to a lower dose rate.

5. Summary and Conclusions

We investigated the electrochemical behavior and surface films that formed on Alloy 600 with and without 100 ppb of zinc in PWR primary water. A combination of electrochemical tests and electron microscopy were conducted on samples immersed for 4 h at a temperature of 320 °C, which simulated the nuclear reactor conditions. Potentiodynamic polarization tests and 4 h of potentiostatic polarization tests indicated that 100 ppb of aqueous zinc lowered Alloy 600's oxidation rate. A combination of SEM, STEM imaging, and EDS indicated that a duplex surface film was formed on Alloy 600. The same Cr-rich IL of Cr_2O_3 and/or CrOOH formed with and without zinc. Zinc had a significant effect on the outer layer (OL). In the absence of zinc, the OL consisted of Ni-rich whiskers that formed a porous, discontinuous layer. In PWR PW with 100 ppb of zinc, the OL was Ni-rich with a significant amount of zinc and was dense and more continuously covered the IL.

Previous EIS studies indicated that zinc's effect on the oxidation rate after 4 h of immersion was not caused by decreases in metal oxidation reactions at the alloy/IL interface. It was reported that zinc's effect on the corrosion rate after very long immersion times was attributed to zinc decreasing the ion transport through the IL. In contrast, our EIS data indicated that the presence of zinc did not affect the ion transport through the IL, which was consistent with our not finding any zinc in the IL. Instead, our EIS studies indicated that after 4 h of immersion, zinc decreased the corrosion rate by decreasing the release of Ni^{++} from the IL into the electrolyte. The presence of zinc in the water promoted the formation of a nearly pore-free OL that continuously covered the IL. In contrast, in the absence of zinc, the porous outer layer allowed nickel ions to directly dissolve out of the IL and into the aqueous electrolyte.

Supplementary Materials: The following supporting information can be downloaded at: https://www.mdpi.com/article/10.3390/cmd4010005/s1. Figure S1: (a) Bright-field cross-sectional image of Alloy 600 polarized at -700 mV in PWR PW with no zinc. (b) EDS map of nickel, iron, and platinum. (c) EDS map of nickel, chromium, and platinum. (d) EDS map of region of narrow width pictured in (c). (e) Integrated intensities of elements in region of narrow width. Figure S2: (a) Bright-field cross-sectional image of Alloy 600 polarized at −223 mV in PWR PW with no zinc. (b) EDS map of nickel, iron, and platinum. (c) EDS map of nickel, chromium, and platinum. (d) EDS map of region of narrow width pictured in (c). (e) Integrated intensities of elements in region of narrow width. Figure S3: (a) Bright-field cross-sectional image of Alloy 600 polarized at −700 mV in PWR PW with 100 pp of zinc. (b) EDS map of nickel, iron, and platinum. (c) EDS map of nickel, chromium, and platinum. (d) EDS map of region of narrow width pictured in (c). (e) Integrated intensities of

elements in region of narrow width. Figure S4: (a) Bright-field cross-sectional image of Alloy 600 polarized at −223 mV in PWR PW with 100 ppb of zinc. (b) EDS map of nickel, iron, and platinum. (c) EDS map of nickel, chromium, and platinum. (d) EDS map of region of narrow width pictured in Figure (c). (e) Integrated intensities of elements in region of narrow width. Table S1: Composition comparison of Cr-rich layers and alloy substrates formed with and without zinc at −550mV. Table S2: Compositions of 14 OLs at −700 mV and −550 mV with and without 100 ppb of zinc. Figure S5: Influence of potential on the real component of impedance of Alloy 600 in PWR PW with no Zn. Figure S6: Influence of potential on the real component of impedance of Alloy 600 in PWR PW with Zn. Figure S7: Influence of potential on the imaginary component of impedance of Alloy 600 in PWR PW with no Zn. Figure S8: Influence of potential on the imaginary component of impedance of Alloy 600 in PWR PW with Zn. Figure S9: Fitting the modulus and phase angle of the impedance of the EC to the measured impedance at −695 mV in Zn-free PWR PW. After the EIS, the sample's surface film was investigated via SEM and TEM. Figure S10: Fitting the modulus and phase angle of the impedance of the EC to the measured impedance at −690 mV in PWR PW with 100 ppb of Zn. After the EIS, the sample's surface film was investigated via SEM and TEM. Figure S11: Fitting the modulus and phase angle of the impedance of the EC to the measured impedance at −565 mV in Zn-free PWR PW. After the EIS, the sample's surface film was investigated via SEM and TEM. Figure S12: Fitting the modulus and phase angle of the impedance of the EC to the measured impedance at −570 mV in PWR PW with 100 ppb of Zn. After the EIS, the sample's surface film was investigated via SEM and TEM. Figure S13: (a–c) Influence of zinc and potential on the capactive elements of the EC.

Author Contributions: The experiments described in this paper were performed by Y.J. as part of her Ph.D. research, which was supervised by T.M.D. and K.C.B. analyzed the TEM/EDS results. The initial draft of this paper was written by T.M.D.; K.C.B. and Y.J. contributed to writing of the final draft. All authors have read and agreed to the published version of the manuscript.

Funding: The first two years of our five-year program were supported by the Electric Power Research Institute of Palo Alto, CA. The funds allowed the refurbishment of our high-pressure water loop and autoclave to accommodate testing with PWR PW at 320 °C and initial EIS measurements. The contract was administered by Raj Pathania and Peter Chou.

Data Availability Statement: Raw EDS and EIS data from this work is free for download and can be found at DOI 10.5281/zenodo.7530292.

Acknowledgments: Christopher Kumai designed our high-temperature, high-pressure, all-titanium water loop and autoclave. The electron microscopy was conducted at the National Center for Electron Microscopy at the Molecular Foundry, Lawrence Berkeley National Laboratory. We are very grateful for the assistance provided by Chengyu Song (TEM), John Turner (FIB), and Andy Minor. Work at the Molecular Foundry was supported by the Office of Science, Office of Basic Energy Sciences, of the U.S. Department of Energy under Contract No. DE-AC02-05CH11231. The samples of Alloy 600 were obtained from material provided by Peter L. Andresen (Ret.) of the GE Global Research Center, who also contributed to the design of our high-temperature, high-pressure water loop.

Conflicts of Interest: The authors declare no conflict of interest.

Appendix A. Preliminary Examination of EIS: Graphical Analyses, DC Current Density during EIS, and Equilibrium Potentials

Appendix A.1. Preliminary Inspection of Impedance Spectra

Graphical analysis is an effective procedure for initiating the interpretation of impedance spectra [47]. As mentioned in the Results section, the overall shapes of the Nyquist plots presented in Figures 7 and 8 indicated that the EIS formed three groups, which were named 700, 550, and 223 based on the approximate values of the potentials of the samples investigated via electron microscopy.

In addition to the shapes of the Nyquist plots, the polarity and magnitude of the DC current density during the measurement of impedance, which are listed in Table A1, helped to identify the processes that contributed to the impedance.

Table A1. DC Current during Electrochemical Impedance Tests.

	Run 1	**Run 2**	**Run 3**
Potential (mV vs. SHE)	**A/cm^2**	**A/cm^2**	**A/cm^2**
−743	-1.77×10^{-7}	-8.70×10^{-7}	-1.40×10^{-6}
−723	-1.90×10^{-7}	-2.70×10^{-7}	1.07×10^{-7}
−673	-9.63×10^{-8}	6.67×10^{-7}	-4.60×10^{-8}
−623	4.18×10^{-8}	9.86×10^{-7}	1.84×10^{-8}
−573	5.02×10^{-8}	9.88×10^{-7}	1.03×10^{-7}
−523	3.90×10^{-7}	7.08×10^{-7}	3.21×10^{-7}
−423	1.13×10^{-6}	1.07×10^{-6}	1.48×10^{-6}
−323	2.86×10^{-6}	2.30×10^{-6}	4.18×10^{-6}
−223	6.34×10^{-6}	5.13×10^{-6}	1.06×10^{-5}

The steady-state DC current density as a function of the DC potential during three measurements of EIS, which are listed in Table A1, along with the plot of steady-state DC current density versus potential, which is presented in Figure 6, indicated that at −743 mV and −723 mV, the rates of the oxidation and reduction reactions were comparable, meaning that both the oxidation and reduction reactions contributed to the impedance measured at −743 mV and −723 mV.

The equilibrium potentials of particular reactions also helped to identify reactions that might have occurred during the impedance measurements. For example, based on our calculated value of pH at 320 °C of 7.2, the equilibrium potential of the hydrogen reduction reaction was calculated as −723 mV vs. SHE (the biggest factor contributing to the uncertainty of the value of −723 mV was the fugacity of hydrogen, which we calculated as 0.0055 atm at 320 °C). Thus, it was expected that the hydrogen reduction reaction (HRR) contributed to the impedance at −743 mV and −723 mV and that at potentials of −673 mV and more positive, we expected the faradaic impedance to be primarily associated with oxidation reactions.

In summary, the combined input of the shapes of the Nyquist plots, the values of the DC current density during the EIS measurements, the steady-state polarization curve, and the calculated values of the equilibrium potentials of the relevant redox reactions provided a preliminary characterization of the impedance spectra as is presented in Table A2. In particular, the calculated value of the equilibrium potential of the HRR, the shapes of the Nyquist plots, and the DC current densities during the EIS suggested three groups of the impedance spectra measured at potentials from −743 mV to −223 mV. In particular, Group 700 consisted of spectra measured at −743 mV and −723 mV. Here, the reduction reaction was dominant, but both the electrochemical reduction reaction and the oxidation reaction were significant. Group 550 was composed of spectra measured at potentials of −623 mV and −573 mV, and the EIS was expected to be dominated by the oxidation reaction. Finally, the spectra at −423, −323, and −223 composed Group 230, which was reflective of a different oxidation reaction from that of Group 550. This division of spectra into three groups of similarly shaped Nyquist plots indicated that three different ECs were required to represent the electrochemical behavior of Alloy 600 over the wide range of potentials from −743 mV to −223 mV.

Table A2. Grouping of Impedance Spectra Based on the Shapes of Nyquist Plots, Magnitude and Polarity of DC Current Density, and Equilibrium Potentials.

Spectra with Similarly Shaped Nyquist Plots	**Spectra with Similar Values of i_{DC}**	**Electrochemical Reactions Contributing to EIS**
−743 mV, −723 mV	−743 mV, −723 mV	HRR and Oxidation of Alloy
−673 mV, −623 mV, −573 mV, −523 mV	−673 mV, −623 mV, −573 mV, −523 mV	Oxidation Reaction #1 of Alloy
−423 mV, −323 mV, −223 mV	−423 mV, −323 mV, −223 mV	Oxidation Reaction #2 of Alloy

A more detailed analysis began with the spectra of Group I.

Appendix A.2. Detailed Examination of EIS

Appendix A.2.1. EIS at −743 mV and −723 mV

Appendix A.2.1.1. Overview

Different representations of EIS at −743 mV are presented in Figure A1a,b,c,d. As summarized in Table A3, three ranges of frequency were identified: $0.002 < f \leq 0.01$, $0.02 \leq f \leq 0.4$, and $10 \leq f \leq 4000$. In each range, the impedance was dominated by a particular electrochemical reaction or by non-Faradaic processes that included diffusion of the electrochemical reactions' reactants/products. The same three ranges of frequency are contained in each of the representations of the EIS shown in Figure A1a,b,c,d. The solution's ohmic impedance and the impedance associated with the OL of the surface film dominated the phase angle and the real component of impedance at $4000 \leq f \leq 60{,}000$, as was discussed in Section 3.4.3 of the Results.

Table A3. Summary of EIS of No-Zn Test at −743 mV.

Freq. Range	Nyquist Plot	Log Im. vs. Log Freq.	Phase Angle vs. Log Freq.	Log Real vs. Log Freq.	Components of EC
0.002 < Freq ≤ 0.01 Hz	Straight line of slope +0.92	Straight line of slope −0.49	Monotonically decreasing angle (−22° to −32°) with decreasing freq.	Straight line of slope −0.25 |Im| < |Re|	R + Z_W
0.02 Hz < Freq ≤ 0.4	Portion of a circular arc	Straight line of slope −0.36	Monotonically decreasing angle (−11° to −20°) with decreasing freq.	Gentle curve with negative slope	Ra | |Ca R + Z_W
10 Hz < Freq. ≤ 4000 Hz	Only info is Re—Constant and Im–0	Inverted V-shape with max. at 25 Hz; high-freq. side is str line of slope of −0.74; low-freq. side overlaps with Group II	V-shape with minimum at 40 Hz	Monotonically decreasing from 10 Hz to 500 Hz; constant at freqs. greater than 500 Hz	R | |C_{DL}

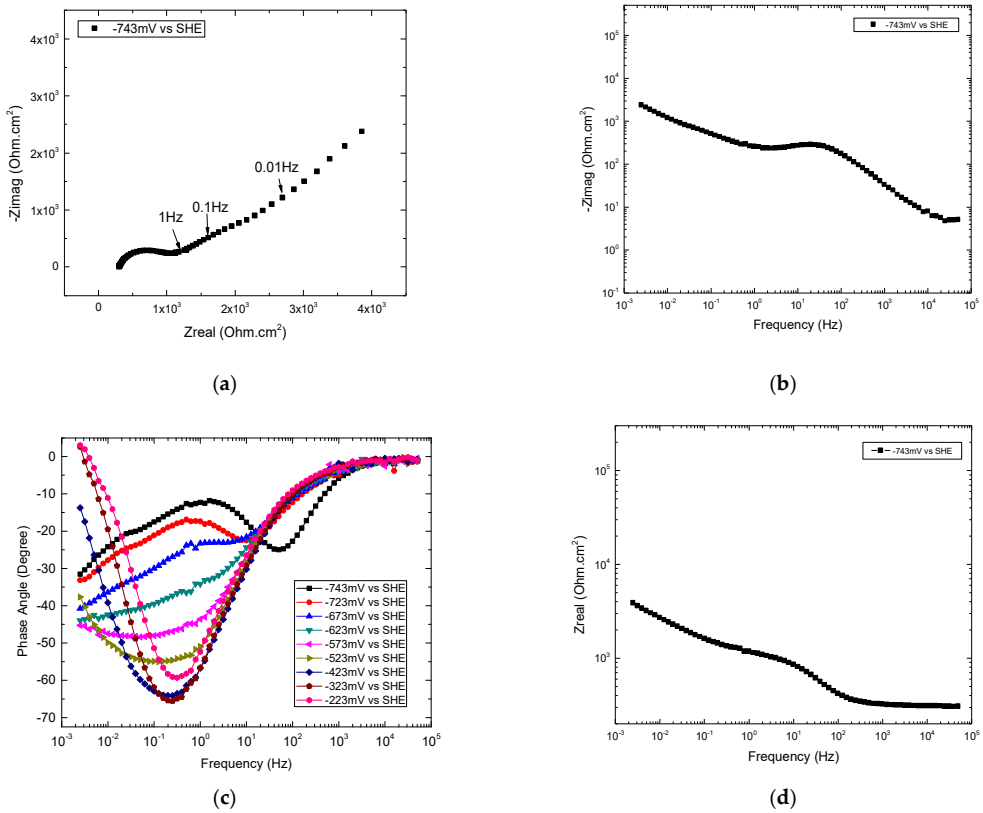

Figure A1. (**a**–**d**) EIS of Alloy 600 in no-Zn test at −743 mV. Each figure includes the same three ranges of frequency: 0.002–0.01 Hz, 0.02–0.4 Hz, and 10–4000 Hz. Specific features characterized each range of frequency. (**a**) Nyquist plot; (**b**) Log imag. vs. log freq.; (**c**) phase angle vs. log freq.; (**d**) log real vs. log freq.

The impedance behaviors in the spans of frequencies in between the first and second ranges, the second and third ranges, and the third and fourth ranges were the result of overlapping of the behaviors of the first and second ranges, the second and third ranges, and the third and fourth ranges, respectively.

The characteristics of the impedance within each of the three ranges of frequency are listed in Table A3. The right-most column lists the circuit elements suggested by the impedance behavior.

Appendix A.2.1.2. 0.002 Hz $\leq$ Frequencies $\leq$ 0.01 Hz at −743 mV

As indicated in the first row of Table A3, the combination of the shapes of the Nyquist plot (straight line of slope +0.92) and the graph of log im. vs. log freq. (straight line of slope −0.49) strongly suggested that the impedance contained a Warburg element. Ideally, the impedance of a Warburg element (W) for a quasi-infinite medium is characterized by a Nyquist plot with a slope of +1.0 (i.e., $|\mathrm{Im}| = |\mathrm{Re}|$) and a plot of log im. vs. log freq. of slope −0.50 (i.e., $\mathrm{Im} = -s/j(2\pi f)^{1/2}$. The fact that the phase angle was not equal to the ideal value of 45° and that $|\mathrm{Re}|$ was greater than $|\mathrm{Im}|$ rather than the ideal behavior of $|\mathrm{Re}| = |\mathrm{Im}|$ suggested another contribution to Re in addition to the Warburg impedance. Given that the hydrogen reduction reaction (HRR) was the dominant electrochemical process taking place at the applied DC potential of −0.743 mV, the simplest addition to make that consistent with the measured spectra was a resistance in series with the diffusive impedance, and the added resistance was most likely associated with the electron transfer steps of the HRR.

Appendix A.2.1.3. 0.02 Hz $\leq$ Frequencies $\leq$ 0.4 Hz at −743 mV

The second row of Table A3 lists the dominant features of the four representations of the EIS in the frequency range of 0.02 Hz to 0.4 Hz. The Nyquist plot was shaped like a segment of a circular arc; the plot of log im. vs. log freq. formed a straight line of slope −0.36; the phase angle monotonically decreased with a decreasing frequency; and the log re. vs. log freq. exhibited a gentle curvature that transitioned between the negatively sloped line at frequencies $\leq$ 0.02 Hz and the nearly horizontal line at frequencies $\geq$ 0.4 Hz.

There were at least two sets of circuit elements that were consistent with the impedance behavior exhibited in the frequency range of 0.02 Hz–0.4 Hz. One was a resistor in parallel with a constant phase element (CPE), which produced a half-loop in the Nyquist plot and a straight line of slope -a (where $0 < a \leq 1$) in the plot of log im. vs. log frequency. The results summarized in the second row of Table A3 were consistent with the impedance of a resistor in parallel with a non-ideal capacitance. The slope of log im. vs. log freq. of a resistor in parallel with an ideal capacitor was −1.0, which was considerably different from the measured value of −0.36. That the slope of the plot of log im. vs. log freq. was a constant suggested the resistor was in parallel with a CPE. However, the phase angle was not constant, which either ruled out a CPE or was a consequence of several contributions to the impedance. Our attempts to fit the measured EIS at 0.002 Hz $\leq$ freq. $\leq$ 0.4 Hz to the calculated impedance of the EC that contained a CPE in parallel with a resistor were unsuccessful.

A second set of circuit elements that were consistent with the impedance behavior was a resistor in series with the Warburg impedance of a finite-size medium. The slope of −0.36 of log im. vs. log freq. was the result of overlapping of the impedances of the two parallel arrangements of R and W in series. This selection provided a much better fit to our data, as is indicated in Figures 13, S7 and S9.

Appendix A.2.1.4. 10 Hz $\leq$ Frequencies $\leq$ 4000 Hz at −743 mV

The shapes of the four representations of EIS over the frequency range of 10 Hz to 4000 Hz are listed in the third row of Table A3. Due to the high range of values of frequency, no information was provided by the Nyquist plot; the plot of log im. vs. log freq. exhibited

a portion of an inverted-V shape; the phase angle vs. log freq. formed a V-shape; and the plot of log re. vs. log freq. decreased as the frequency increased from 10 Hz to 500 Hz and was constant at frequencies greater than 500 Hz. The impedance behavior was consistent with the impedance of a resistance in parallel with a CPE in which alpha = −0.74. We set the characteristic frequency equal to 50 Hz, which was the frequency of the local minimum of the phase angle plot (see Figure A1c) and the frequency of the maximum of im. in the circular arc of the Nyquist plot and then set R = 500 ohm·cm^2; solving for C then indicated that C ≈ 6 μF/cm^2.

Appendix A.2.1.5. Summary of Graphical Analyses of EIS at −743 mV

Combining the results (from Table A3) of the impedance measured over four ranges of frequency indicated that the EC of the reduction and oxidation reactions was that presented in Figure A2. The impedance consisted of two parallel arrays of a resistor in series with a Warburg impedance. The fit of the equivalent circuit to the measured impedance is considered in the following section.

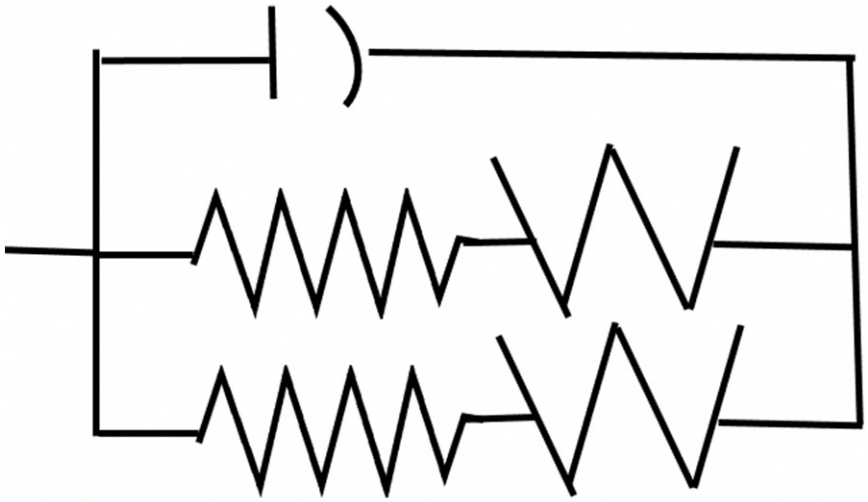

Figure A2. Preliminary equivalent circuit for the low-frequency range (<10 Hz) of EIS at −743 mV.

Appendix A.2.1.6. Fit of the EC based on GA to the measured EIS

The EC derived from the graphical analysis described above provided good but not perfect fits with the data. Often, one set of values of the circuit elements that optimized the fit of one representation of the impedance (e.g., phase angle vs. log frequency) provided an inadequate fit with other representations of the impedance (e.g., log re. and log im. vs. log frequency). Apparently, elements were missing from the EC sketched in Figure A2. Presumably, the missing elements made contributions to the impedance that were too subtle to be detected in the graphical analysis. It was likely that the missing contributions partially overlapped the frequency range in which elements already included in the EC were dominant.

The results of the SEM/TEM were examined for clues to the identities of the missing circuit elements. The surface films contained a continuous, dense IL of Cr_2O_3 and a porous OL. The structure of the OL depended on whether the tests were conducted with or without aqueous zinc ions. As stated in Section 3.4.3 of the Results, the NiO nanowires that acted as a porous OL on the no-zinc samples (polarized at potentials more negative than −423 mV) introduced a parallel arrangement of a resistor and CPE with a high characteristic frequency. The samples polarized with zinc in the electrolyte had an OL that was significantly denser than the array of NiO nanowires. Consequently, for the samples tested with zinc, an R | | CPE was added in series with the ohmic resistance of the electrolyte.

With the additions of R | | CPE to the ECs of the Zn tests and the no-Zn tests, excellent fits to our measured EIS were achieved. Thus, the final ECs, which were based on the graphical analyses and TEM/SEM results, are presented in Figure 12a,b. The quality of the

fits of the EC to the measured EIS of the Zn test and the no-Zn-test are demonstrated by the plots presented in Figure 13, Figures S7 and S9.

Appendix A.2.2. EIS at −623 mV and −573 mV

Appendix A.2.2.1. Overview

The Nyquist plots at −623 mV and −573 mV were thought to best represent the behavior of Group 550 because the Nyquist plot at −673 mV was a blend of the impedances that were dominant in Groups 700 and 550, and the Nyquist plot at −523 mV was a blend of Groups 550 and 230.

At first glance, the Nyquist plots of the no-Zn tests at −623 mV and −573 mV (presented in Figures 7 and 8) appeared to consist of a single straight line with a slope of +1 and, as was shown further ahead in the report, the plots of log im. vs. log freq. seemed to consist of a single straight line of slope −1/2. However, the inserts in Figures 7 and 8 indicated that there was a portion of a circular arc at higher frequencies in the Nyquist plot, and a closer inspection of the Log im. vs. log freq. indicated subtle but important perturbations of the straight lines. Similar features were present in the plot of log im. vs. log freq. for the Zn tests and were more pronounced, so we decided to begin with the analysis of the results of the Zn tests.

Appendix A.2.2.2. Frequencies ≤ 1.4 Hz at −623 mV

As summarized in Table A4, the different representations of the impedance vs. frequency indicated there were three ranges of frequency in which specific behavior characterizes the impedance. The shapes of the different representations of the impedance spectra were the same for the Zn tests conducted at −623 mV and −573 mV, so in the interest of brevity, only the results at −623 mV are discussed.

Table A4. Zn Test Summary of EIS at −623 mV.

Nyquist Plot	Log Im. vs. Log Freq.	Phase Angle vs. Log Freq.	Log Re. vs. Log Freq.
	0.002 Hz < Freq. ≤ 0.04 Hz Slope = −0.46		0.002 Hz < Freq. < 5 Hz Slope = −0.41
0.02 Hz < Freq. ≤ 0.4 Hz Slope = +0.84	0.04 Hz < Freq. ≤ 1.4 Hz Slope = −0.42	0.002 Hz < Freq. ≤ 1.0 Hz Phase angle = 39° − 35°	
	1.4 Hz < Freq. ≤ 40 Hz Gradual, downward bend		
Segment of circular arc starts at 1–2 Hz	40 Hz < Freq. < 2000 Hz Slope = −0.76	2.4 Hz < Freq. ≤ 1000 Hz Smooth decrease to 0°	
	1.4 Hz < Freq. ≤ 4000 Hz V-shaped with slope of ±0.76		
	4000 Hz < Freq. Imped. = Resist. of 5 ohm	Phase angle = 0°	200 Hz < Freq. Re = 550 ohms

At 0.0025 Hz, Re. ≈ 2.1×10^4 and Im. ≈ 1.9×10^4, therefore $R_t \approx 2 \times 10^3$.

Consider first the lowest range of frequencies, which is described in the first row of Table A4. A portion of the Nyquist plot of the Zn test at −623 mV is presented in the insert of Figure A3a. Over the frequency range of 0.02 Hz ≤ f ≤ 0.4 Hz, the Nyquist plot formed a straight line of slope of +0.84. The Nyquist plot of the entire spectrum (Figure A3a) indicated the straight line extended to the lowest frequency tested of 0.002 Hz. Over a similar but wider range of frequencies (0.002 ≤ f ≤ 1.4 Hz), the plot of log im. vs. log freq., which is presented in Figure A3b, formed a straight line of slope of −0.46 and, as shown in Figure A3c, the plot of phase angle vs. log freq. (0.002 < f < 1.0 Hz) indicated the phase angle was nearly constant and varied by only a few degrees (from 39° to 35°) over the range of frequencies. In addition, as shown in Figure A3d, over a still wider range of frequencies (0.002 < f < 5 Hz), the plot of log re. vs. log freq. exhibited a straight line of slope of −0.41,

which was approximately the same value of the slope of log im. vs. log freq. Collectively, the observations listed in the first row of Table A3 indicated the dominant impedance was a Warburg impedance (i.e., the diffusive impedance of an infinitely sized medium).

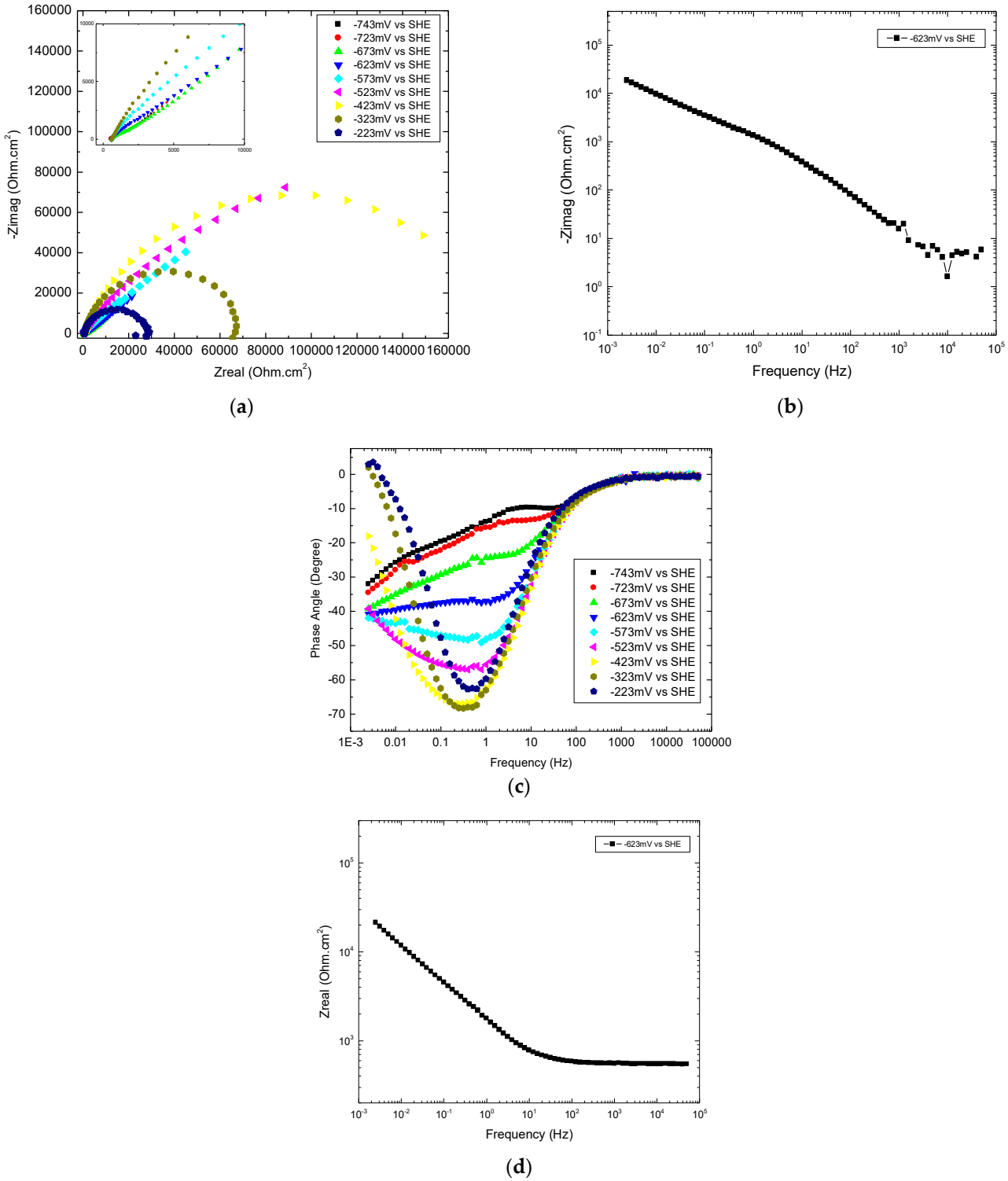

Figure A3. (**a**) Nyquist plot of Zn tests as a function of DC potential. Insert presents high-frequency portions of the Nyquist plots. (**b**) Plot of log im. Vs. log freq. of Zn test at −623 mV. (**c**) Phase angle as a function of frequency and potential of Zn test. (**d**) Log re. vs. log freq. of Zn test at −623 mV.

Ideally, the Nyquist plot of a Warburg impedance has a slope of +1.0 rather than the observed value of +0.84. Similarly, for a Warburg impedance the ideal value of the real component (Re) of impedance was equal to the value of Im. Instead, as shown in Table A5, the difference [Re—Im] was approximately equal to 1000 ohm·cm^2 at frequencies $\leq$ 0.1 Hz (the value at frequencies of 1 and 5 Hz is discussed below). The slope of +0.84 and the non-zero difference of [Re—Im] were attributed to the sum of the two resistances (R_{OX} + R_s = 1000 ohm·cm^2) that were in series with the Warburg impedance. R_s was the ohmic resistance of the electrolyte and, from the high-frequency region of log re. vs. log freq., was equal to 550 ohm·cm^2. The value of R_{OX} was obtained by comparing the value of the difference ([Re—Im]) at 0.002 Hz and 0.1 Hz to the value at 1 Hz and 5 Hz. At 0.002 Hz to 0.1 Hz, [Re—Im] was equal to R_{OX} + R_s; and at 1 Hz to 5 Hz, [Re—Im] was equal to R_s.

Table A5. The Difference ([Re—Im]) in the Frequency Range of 0.0025 Hz $\leq$ f $\leq$ 5 Hz in Zn Test at a Potential of −623 mV.

Frequency	Re	Im	[Re—Im]
0.0025 Hz	2.1×10^4	2.0×10^4	1000 $\approx$ R_{OX} + R_S
0.1 Hz	4.4×10^3	3.3×10^3	1100 $\approx$ R_{OX} + R_S
1 Hz	1.8×10^3	1.3×10^3	500 $\approx$ R_S
5 Hz	970	600	370 $\approx$ R_S

Appendix A.2.2.3. 1.4 Hz $\leq$ Frequencies $\leq$ 40 Hz at −623 mV

Next, we considered the impedance at frequencies greater than 1.4 Hz. The results are summarized in the second row of Table A4. As shown in Figure A4, which is a higher-frequency portion of the Nyquist plot shown in Figure 8, the Nyquist plot changed from a straight line at frequencies less than 1 Hz to a segment of a circular arc starting at a frequency of 1 to 2 Hz. due to the limited frequency-resolution at high frequencies, the Nyquist plot did not provide much information on impedance at frequencies above several Hz, so the upper frequency limit of the arc was not discernable from the Nyquist plot. Information about the impedance at frequencies above 1 Hz was provided by the plot of log im. vs. log frequency, which is presented in Figure A5.

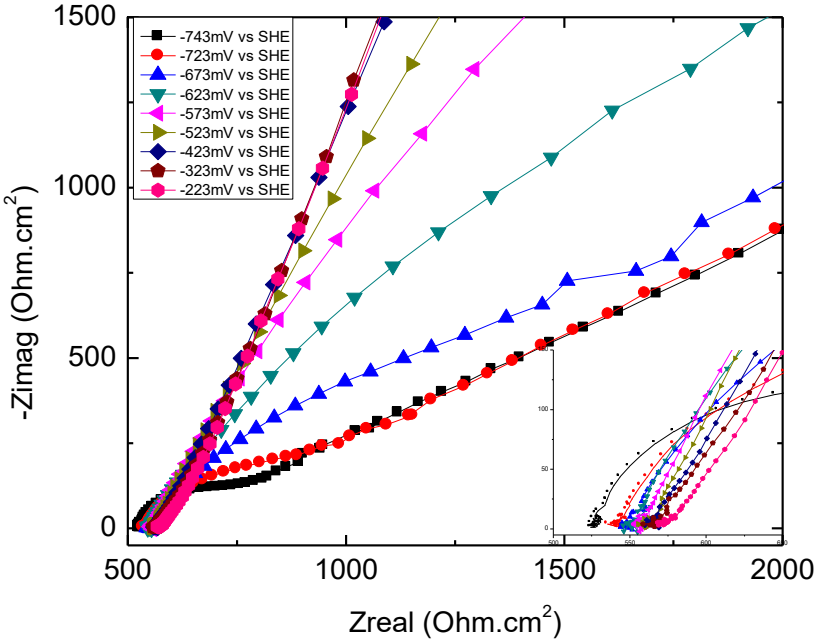

Figure A4. The curvatures of the Nyquist plots of −623 mV and −573 mV in the higher range of frequencies that are depicted represent portions of circular arcs.

In Figure A5, the plot of log im. vs. log freq. gradually curves downwards over 1.4 Hz < f < 40 Hz and transitions to a straight line that extends over the range of 40 < f < 2000 Hz with a slope of −0.76. In this high range of frequencies, the phase angle and re. were dominated by the electrolyte's ohmic impedance and, consequently, provided little information about the faradaic impedance. The observations of the Nyquist plot and the plot of log im. vs. log frequency suggested that in the range of frequencies of 1.4 Hz < f < 40 Hz, the impedance was represented by a CPE in parallel with a resistance R_{ox}. The value of the exponent alpha of the CPE was −0.76.

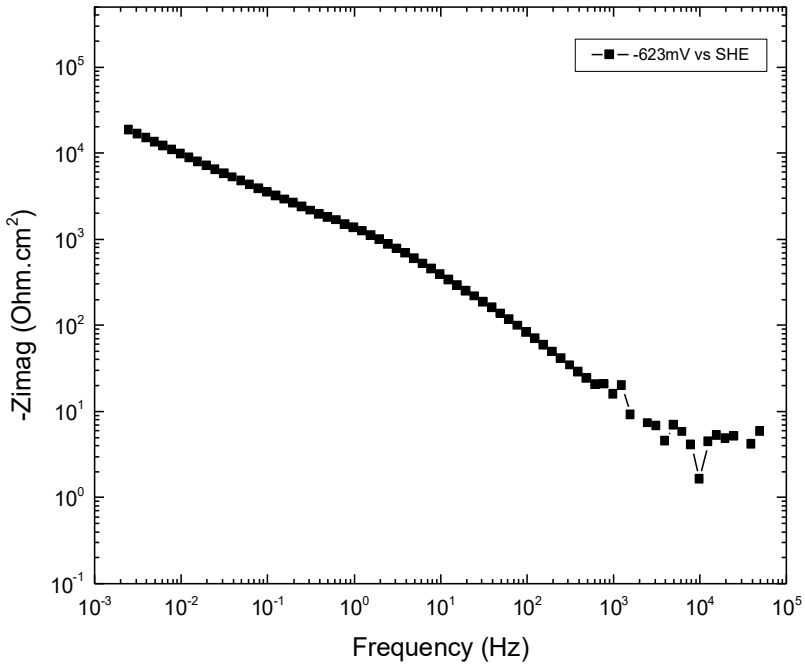

Figure A5. Plot of Log Im. vs. Log Frequency of Zn Test at −623 mV.

The following reasoning suggested that the transition in the dominant imaginary component of impedance from Warburg to a CPE as the frequency was increased from <1.4 Hz to >1.4 Hz indicated the Warburg and CPE were in parallel. The frequency dependence of Im(Z_w) was $f^{-1/2}$ and of Im(CPE) was $f^{-0.76}$, which indicated that the magnitude of Im(Z_w) was less than that of Im(CPE) as frequency tended to zero, and that the magnitude of Im(CPE) was less than that of Im(Z_w) at high values of frequency. The plot of log im. vs. log freq. Indicated that the dominant impedance was that with the lower value, which indicated the Z_w and CPE were in parallel.

The different representations of the impedance spectra also indicated the location of R_{OX} in the overall arrangement of the equivalent circuit's three components of Z_w, CPE, and R_{OX}. Returning to Table A5, the values of the difference ([Re—Im]) as a function of frequency indicated that at −623 mV, the resistance R_{OX}, which was in series with the Warburg impedance, did not contribute to the value of Re at frequencies above 1 Hz. That is, the EC for 1.4 Hz ≤ frequencies ≤ 40 Hz consisted of a CPE that was in parallel with the series combination of R_{OX} and the Warburg impedance Z_w (as opposed to an EC in which R_{OX} was in series with the parallel combination of the CPE and the Warburg impedance).

Preliminary attempts to fit the impedance of the EC to the measured EIS suggested that the EC was missing some elements. That is, the impedance spectrum of the equivalent circuit that qualitatively matched the measured EIS of Alloy 600 in the Zn test at −623 mV (and −573 mV) provided a generally good but less than perfect fit to the measured EIS. We concluded that the EC did not provide an optimum fit of the EIS as presented in the plots of log re., log im., and phase angle vs. log frequency. As was discussed in Appendix A.2.1.6, clues to the missing elements of the EC were obtained from the structure of the surface film as provided by the SEM and TEM results. The most obvious feature of the surface films

not represented by the circuit elements listed in Table A3 was the complex structure of the porous outer layer. The impedance associated with the porous outer layer consisted of a parallel arrangement of a CPE and resistor placed in series with the EC shown in Figure A6. As discussed in the subsection entitled "Low Frequency Impedance—Group 550" of the Results, the EC provided an excellent fit to the measured EIS.

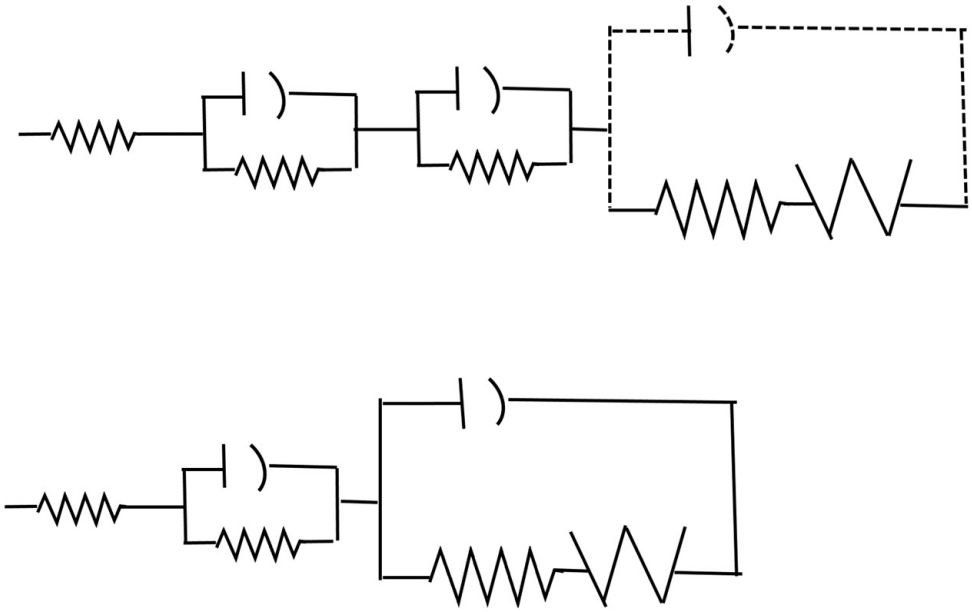

Figure A6. (**top**) Equivalent circuit of no-Zn test of Alloy 600 at −623 mV. (**bottom**) Equivalent circuit of Zn test of Alloy 600 at −623 mV.

Appendix A.2.2.4. Summary of Graphical Analysis of EIS at −623

Graphical analyses of the EIS of no-Zn at −623 mV indicated a nearly identical EC to that of the Zn test. One difference was the failure of the graphical analysis to detect the CPE_{DL} of the no-Zn EIS. The plots of log im. vs. log frequency indicated that this failure was due to the low value of R_{ox} +Z_W that was in parallel with CPE_{DL}.

Appendix A.3. High-Frequency Response

At the highest range of frequencies (4000 ≤ frequency ≤ 60,000), the imaginary component of the no-Zn tests and the Zn tests (Figure A3b) exhibited a nominal value of 5 ohm·cm^2 with some scatter. These results were attributed to the capacitance of the reference electrode.

References

1. Westinghouse Nuclear Services/Engineering Services NS-ES-0089, January 2017. Available online: https://www.westinghousenuclear.com/Portals/O/operating%20plant%20services/engineering/nsss%20system%208%20component%20analysis/NS-ES-0089%20Zinc%20Addition%20Flysheet. (accessed on 1 January 2021).
2. Pathania, R.; Yagnik, S.; Gold, R.; Dove, M.; Kolstad, E. Evaluation of Zinc Addition to Primary Coolant of Farley-2 Reactor. In Proceedings of the 7th International Symposium on Environmental Degradation of Materials in Nuclaer Power Systems–Water Reactors, Breckenridge, CO, USA, 6–10 August 1995; pp. 163–173.
3. Pathania, R.; Cheng, B.; Dove, M.; Gold, R.; Bergmann, C. Evaluation of Zinc Addition to Primary Coolant of Farley-2 Reactor. In Proceedings of the 8th International Symposium on Environmental Degradation of Materials in Nuclaer Power Systems–Water Reactors, Amelia Island, FL, USA, 10–14 August 1997; pp. 379–386.
4. Betova, I.; Bojinov, M.; Kinnunen, P.; Saario, T. Zn Injection in Pressurized Water Reactors–Laboratory Tests, Field Experience and Modeling. In *Research Report No. VTT-R-05511-11*; Zinc Injection Update; Haas, V.C., Perkins, D., Eds.; Technical Research Center of Finland: Otaniemi, Finland, 2011; pp. 1–5.
5. Ocken, H.; Fruzzetti, K.; Frattini, P.; Wood, C.J. Recent Developments in PWR Zinc Injection. In Proceedings of the International Conference on Water Chemistry in Nuclear Reactor Systems, Avignon, France, 22–26 April, 2002.

6. Haas, V.C.; Perkins, D.; Zinc Injection Update. Nuclear Engineering International. Available online: https://www.neimagazine.com/features/featurezinc-injection-update/ (accessed on 1 January 2021).
7. Marble, W.J. An Overview of Zinc Addition for BWR Dose Rate Control. In Proceedings of the Third International Workshop on the Implementation of ALARA at Nuclear Power Plants, Long Island, NY, USA, 8–11 May 1994; pp. 67–84.
8. Kawamura, H.; Hirano, H.; Shirai, S.; Takamatsu, H.; Matsunaga, T.; Yamaoka, K.; Oshinden, K.; Takiguchi, H. Inhibitory Effect of Zinc Addition to High-Temperature Hydrogenated Water on Mill-Annealed and Prefilmed Alloy 600. *Corrosion* **2000**, *56*, 623–637. [CrossRef]
9. Ziemniak, S.E.; Hanson, M. Zinc Treatment Effects on Corrosion Behavior of Alloy 600 in High Temperature, Hydrogenated Water. *Corros. Sci.* **2006**, *48*, 3330–3348. [CrossRef]
10. Alvial, M.G.; Neves, C.F.C.; Schvartzman, M.M.A.M.; Quinan, M.A.D. Electrochemical Evaluation of Zinc Effect on the Corrosion of Nickel Alloy in PWR Solutions with Increasing Temperature. In Proceedings of the 2007 International Nuclear Atlantic Conference–INAC, Santos, Brazil, 30 September–5 October 2007.
11. Esposito, J.N.; Economy, G.J.; Byers, W.A.; Esposito, J.B.; Peinent, F.W.; Jacko, R.J.; Bergmann, C.A.R. The Addition of Zinc to Primary Reactor Coolant for Enhanced PWSCC Resistance. In *Proceedings of the Fifth International Conference on Environmental Degradation of Materials in Nuclear Power Systems–Water Reactors*; American Nuclear Society: LaGrange Park, IL, USA, 1991.
12. Gold, B. *Materials Reliability Program: Effect of Zinc Additions on Mitigation of Primary Water Stress Corrosion Cracking of Alloy 600 (MRP-78)*; EPRI: Palo Alto, CA, USA, 2002; P. *100* 3522.
13. Kawamura, H.T.; Hirano, H.; Yamaoka, K.; Shirai, S.; Oshindfen, K.; Takamatsu, H.; Matsunaga, T.; Takiguchi, H. The Effect of Zinc Addition to Simulated PWR Primary Water on the PWSCC Resistance, Crack Growth Rate and Surface Oxide Film Characteristics on Prefilmed Alloy 600. *Corrosion* **1998**, *98*, 141.
14. Andresen, P.L.; Hickling, J.; Ahluwalia, K.S.; Wilson, J.A. Effects of PWR Water Chemistry on PWSCC of Ni Alloys. In Proceedings of the 13th International Conference on Environmental Degradation of Materials in Nuclear Power Systems, Whistler, BC, Canada, 19–23 August 2007.
15. Gordon, B.M.; Garcia, S. Effect of Water Purity on Intergranular Stress Corrosion Cracking of Stainless Steel and Nickel Alloys in BWRs. In Proceedings of the Fontevraud 7 Contributions of Materials Investigations to Improve the Safety and Performance of LWRs, Avignon, France, 26–30 September 2010.
16. Andresen, P.L.; Angeliu, T.M. Effect of Zinc Additions on the Stress Corrosion Crack Growth Rates of Sensitized Stainless Steel, Alloy 600 and Alloy 182 Weld Metal in 288°C Water. *Corrosion* **1995**, *95*, 410.
17. Angeliu, T.M.; Andresen, P.L. Effect of Zinc Additions on the Oxide Rupture Strain and Repassivation Kinetics of Fe-base Alloys in 288 °C Water. *Corrosion* **1995**, *95*, 411.
18. Bojinov, M.; Galtayries, A.; Kinnuneu, P.; Machet, A.; Marcus, P. Estimation of Parameters of Oxide Film Growth on Ni-Based Alloys in High Temperature Water Electrolytes. *Electrochim. Acta* **2007**, *52*, 7475–7483. [CrossRef]
19. Abraham, G.J.; Kain, V.; Dey, G.K.; Raja, V.S. Stabi;ity of Oxide Film Formed at Different Temperatures on Alloy 600 in Lithiated Environment. *J. Nucl. Mater.* **2013**, *437*, 188–195. [CrossRef]
20. Lai, W.-K.; Szklarska-Smialowska, Z.W. Effect of Heat Treatment on the Behavior of alloy 600 in Lithiated Water Containing Dissolved Hydrogen at 25–350 °C. *Corrosion* **1991**, *47*, 40–47. [CrossRef]
21. Szklarska-Smialowska, Z.; Lai, W.-K.; Xia, Z. oxide Films Formed on Alloy 600 in Lithiated Water at 25° to 350 °C. *Corrosion* **1990**, *46*, 853–860. [CrossRef]
22. Kim, D.-J.; Kwon, H.-C.; Kim, H. Effect of Solution Temperature and the pH on the Electrochemical Properties of the Surface Oxide Film Formed on Alloy 600. *Corros. Sci.* **2008**, *50*, 1221–1227. [CrossRef]
23. Huang, J.; Wu, X.; Han, E.-H. Influence of pH on the Electrochemical Properties of Passive Films Formed on Alloy 690 in High Temperature Aqueous Environments. *Corros. Sci.* **2009**, *51*, 2976–2982. [CrossRef]
24. Huang, F.; Wang, J.; Han, E.-H.; Ke, W. Microstructural Characteristics of the Oxide Films Formed on Alloy 690TT in Pure and Primary Water at 325 °C. *Corros. Sci.* **2013**, *76*, 52–59. [CrossRef]
25. Huang, J.; Liu, X.; Han, E.-H. Influence of Zinc on Oxide Films on Alloy 690 in Borated and Lithiated High Temperature Water. *Corros. Sci.* **2011**, *51*, 3254–3261. [CrossRef]
26. Faichuk, M.G. Characterization of the Corrosion and Oxide Film Properties of alloy 600 and Alloy 800. PhD. Thesis, The University of Western Ontario, Ontario, ON, Canada, 2013.
27. Terachi, T.; Totsuka, N.; Yamada, T.; Nakagawa, T.; Deguchi, H.; Horiuchi, M.; Oshitani, M. Influence of Dissolved Hydrogen on Structure of Oxide Film on Alloy 600 Formed in Primary Water of PWRs. *J. Nucl. Sci. Technol.* **2003**, *40*, 509–516. [CrossRef]
28. Peng, Q.; Hou, J.; Sakaguchi, K.; Takeda, Y.; Shoji, T. Effect of Dissolved Hydrogen on Corrosion of Inconel Alloy 600 in High Temperature Hydrogenated Water. *Electrochim. Acta* **2011**, *56*, 8357–8386. [CrossRef]
29. Loucif, A.; Petit, J.-P.; Wouters, Y.; Combrade, P. Effect of Dissolved Hydrogn, Surface Conditions and Composition on the Electronic Properties of the Oxide Films formed on Ni-base Alloys in PWR Primary Water. In Proceedings of the 15th International Conference on Environmental Degradation; Busby, J., Ilevbare, G., Andresen, P., Eds.; TMS: Pittsburgh, PA, USA, 2011; pp. 953–963.
30. Peng, Q.; Shoji, T.; Hou, J.; Sakaguchi, K.; Takeda, Y. Role of Dissolved Hydrogen in Water in Corrosion of Alloy 600 in High Temperature Water. In Proceedings of the 15th International Conference on Environmental Degradation; Busby, J., Ilevbare, G., Andresen, P., Eds.; TMS: Pittsburgh, PA, USA, 2011; pp. 1879–1888.

31. Zhang, Z.; Wang, J.; Han, E.-H.; Ke, W. Influence of Dissolved Oxygen on Oxide Films of Alloy 690TT with Different Surface Status in Simulated Primary Water. *Corros. Sci.* **2011**, *53*, 3623–3635. [CrossRef]
32. Yang, J.; Li, Y.; Macdonald, D.D. Effects of Temperature and pH on the Electrochemical Behavior of Alloy 600 in Simulated PWR Primary Water. *J. Nucl. Mater.* **2020**, *528*, 1–16. [CrossRef]
33. Machet, A.; Galtayries, A.; Zanna, S.; Klein, L.; Maurice, V.; Jolivet, P.; Foucault, M.; Combrade, P.; Scott, P.; Marcus, P. XPS and STM Study of the Growth and Structure of Passive Films in High Temperature Water on a Ni-base Alloy. *Electrochim. Acta* **2004**, *49*, 3957–3964. [CrossRef]
34. Machet, A.; Galtayries, A.; Marcus, P.; Combrade, P.; Jolivet, P.; Scott, P. XPS Study of Oxides Formed on Ni-base Alloys in High Temperature and High Pressure Water. *Surf. Interface Anal.* **2002**, *34*, 197–200. [CrossRef]
35. Voyshnis, S.; Seyeux, A.; Zanna, S.; Martin-Cabanas, B.B.; Couvant, T.; Marcus, P. Oxide Layer Growth on Nickel-base Alloy Surfaces in High Temperature Water and in O_2 Studied by ToF-SIMS with Isotropic Tracers. *Corros. Sci.* **2018**, *145*, 212–219. [CrossRef]
36. Kaufman, L. *Pourbaix Diagrams of Ternary Ni-Cr-Fe Alloys in Water at 325 °C with 2 ppm LiOH and 1200 ppm H3BO3*; EPRI: Palo Alto, CA, USA, 2008.
37. Huang, J.; Wu, X.; Han, E.-H. Electrochemical Properties and Growth Mechanisms of Passive Films on Alloy 690 in High Temperature Alkaline Environments. *Corros. Sci.* **2010**, *52*, 3444–3452. [CrossRef]
38. Bojinov, M.; Kinnunen, P.; Sunduolm, G. Electrochemical Behavior of Nickel-Chromium Alloys in a High temperature Aqueous Electrolyte. *Corrosion* **2003**, *59*, 91–103. [CrossRef]
39. Mintz, T.S. An In-Situ Investigation of the Passive Film on Stainless Steel and Inconal 600 in High Temperature, Pressurized, Impurity Containing Water. Ph.D. thesis, University of California, Berkeley, CA, USA, 2003.
40. Mintz, T.S.; Bhargava, Y.V.; Thorne, S.A.; Chopdekar, R.; Radmilovic, V.; Suzuki, Y.; Devine, T.M. Electrochemical Synthesis of Functionalized Nickel Oxide Nanowires. *Electrochem. Solid State Lett.* **2005**, *8*, D26–D30. [CrossRef]
41. Cliff, G.; Lorimer, G.W. The Quantitative Analysis of Thin Specimens. *J. Microsc.* **1975**, *103*, 203–207. [CrossRef]
42. Wang, F. In-situ Surface Enhanced Raman Spectroscopy Investigation of the Surface Films of Alloy 600 and Alloy 690 in Pressurized Water Reactor–Primary Water. Ph.D. Thesis, Department of Materials Science and Engineering, University of California, Berkeley, CA, USA, 2012.
43. Wang, F.; Devine, T.M. In-situ Surface Enhanced Raman Spectroscopy Investigation of the Surface Films Formed on Nickel and Chromium in High-temperature and High-pressure Water. *At. Energy Sci. Technol.* **2013**, *47*, 7.
44. Wang, F.; Devine, T.M. Corrosion Behavior of Ni-base Alloys of Nuclear Power Steam Generator Tubes in High-Temperature, High-Pressure Water. *Corros. Sci. Prot. Technol.* **2015**, *27*, 19–24.
45. Wang, F.; Devine, T.M. Oxide Films Film Formed on Nickel-based Alloys in simulated PWR Primary Water. *Corros. Sci. Prot. Technol.* **2015**, *27*, 339–344. [CrossRef]
46. Orzem, M.; Tribollet, B. *Electrochemical Impedance Spectroscopy*, 2nd ed.; John Wiley & Sons, Inc.: Hoboken, NJ, USA, 2017; pp. 202–205.
47. Orazem, M.E.; Pébère, N.; Tribollet, B. Enhanced Graphical Representation of Electrochemical Impedance Data. *J. Electrochem. Soc.* **2006**, *153*, B129–B136. [CrossRef]